Symmetry-Protected Topological Optical Lattice Clock

Tianrui Xu,[1,2,3,*] Anjun Chu,[1,2,4] Kyungtae Kim,[1] James K. Thompson,[1] Jun Ye,[1] Tilman Esslinger,[5] and Ana Maria Rey[1,2,†]

[1] *JILA, NIST and Department of Physics, University of Colorado, Boulder, Colorado 80309, USA*
[2] *Center for Theory of Quantum Matter, University of Colorado, Boulder, Colorado 80309, USA*
[3] *Institut Quantique and Département de Physique, Université de Sherbrooke, Sherbrooke, Québec J1K 2R1, Canada*
[4] *Pritzker School of Molecular Engineering, University of Chicago, Chicago, Illinois 60637, USA*
[5] *Institute for Quantum Electronics & Quantum Center, ETH Zurich, 8093 Zurich, Switzerland*

(Received 27 January 2025; accepted 24 June 2025; published 6 August 2025)

We theoretically propose a tunable implementation of symmetry-protected topological phases of matter in a synthetic superlattice, taking advantage of the long coherence time and exquisite spectral resolutions offered by gravity-tilted optical lattice clocks. We describe a protocol similar to Rabi spectroscopy that can be used to probe the distinct topological properties of our system. We then demonstrate how the sensitivity of clocks and interferometers can be protected from unwanted experimental imperfections offered by the underlying topological robustness. The proposed implementation opens a path to exploiting the unique opportunities offered by symmetry-protected topological phases in state-of-the-art quantum sensors.

DOI: 10.1103/h1nh-thg9

I. INTRODUCTION

Recent years have witnessed rapid and exciting new developments of optical lattice clocks (OLCs) with excellent quantum coherence and exquisite spectral resolutions [1–10]. Such platforms are ideal for quantum sensing, and have recently reached clock-measurement precision at 7.6×10^{-21} and near minute-long atomic coherence [6,10], making it possible to precisely measure quantities of small magnitudes, such as the gravitational redshift across a millimeter- to centimeter-length scale [6,7].

In parallel, over the past decades, the rapid development of quantum simulation with cold atomic systems has enabled experimental investigations of topological properties of quantum matter [11,12]. In particular, significant progress has been made to experimentally realize a class of topological states of matter, referred to as "symmetry-protected topological (SPT) phases." This type of quantum matter has the property of being insulating in the bulk (i.e., having a gapped dispersion) while conducting at the boundary (i.e., having a gapless dispersion) as long as a certain global symmetry is preserved. Namely, the SPT phases are robust to perturbations that respect said global symmetry and do not close the bulk gap. A prototypical model of a SPT system is the celebrated Su-Schrieffer-Heeger (SSH) model [13,14]. This model, and its closely related models, such as the Rice-Mele (RM) model [15], have been realized in a variety of settings including superlattices [16–19], momentum-space lattices [20–22], Rydberg atoms [23], and multilevel systems [24]. Many interesting properties and dynamics of the SSH (RM) model have been observed in these experiments, such as soliton or edge state dynamics [20,23,25,26], Zak phase measurements [16,21,27], Thouless pumping [17–19,28], edge-to-edge transport [22], and topological quantum walks [21].

At the moment, however, quantum simulations of topological quantum matter appear to be independent from the field of quantum sensing. While the realization of topological phases is exciting in its own right, what is even more appealing is the potential use of topological robustness to remove the vulnerability of state-of-the-art sensors to unwanted noise while keeping their sensitivity to the desired signal. In fact, state-of-the-art optical lattice clocks are limited by the Dick (sampling) noise of an optical local oscillator, and a protocol that extends the coherent evolution time would be highly valuable. Moreover, even in synchronous comparison between two clocks, which are in principle immune to the Dick noise, at the current 10^5 atoms the differential measurements are still not yet limited by the standard quantum limit (SQL)—the fundamental bound in sensitivity achievable with uncorrelated atoms. Therefore, an urgent current need is to find noise-suppressing protocols to allow current clocks

*Contact author: tianruixc@gmail.com
†Contact author: arey@jilau1.colorado.edu

to operate at the SQL, before implementing strategies to further improve OLCs via quantum entanglement.

Here we propose a possible path forward via topological states that are relatively easy to implement in state-of-the-art noninteracting OLCs [10], which can provide metrological benefits from their underlying topological robustness. More specifically, we discuss a protocol to create the simplest SPT model, the SSH model, in a tilted one-dimensional (1D) OLC [see Fig. 1(a)]. The tilt can come from the gravitational acceleration or other types of acceleration, parallel to the 1D OLC axis [6–8,10].

In our proposed setting, atoms are allowed to tunnel in a highly controlled manner without energy costs, leading to spatially delocalized atomic wave functions across the lattice. In the topologically nontrivial phase, specific observables of interest become insensitive to variations of the Hamiltonian parameters that describe the atom dynamics. Such robustness has already been observed in previous experiments [21]. It originates from the Berry phase [29] (or the geometric phase) that atoms accumulate when moving through the lattice. This is similar to the quantized and nonzero Hall conductivity in certain solid-state systems, where the Hall conductivity is robust against noise and fluctuations in material parameters.

In our system, such topological robustness protects coherences in highly mobile atoms, mitigating the so-far detrimental decoherence from the spin-orbit coupling in tunneling-dominated regimes [30]. It allows clock spectroscopy to be performed in a way that is not only robust to local noise—which averages out as atoms delocalize, but also more resilient to global noise sources compared to standard frozen atoms. Figure 1(b) illustrates how the topological robustness of our system can help suppress the OLCs' sensitivity to Rabi frequency amplitude noise. The upper panel shows how standard Rabi spectroscopy is impacted by the presence of experimentally relevant amplitude noise that we discuss in more detail in Sec. IV. The lower panel shows the robustness to such noise enabled by the "SSH clock spectroscopy" protocol, also discussed in Sec. IV.

Furthermore, we show that the capability of atoms to quickly delocalize, even in the presence of a gravitational tilt, enables our protocol to be useful not only for optical phase estimations, but also as a lattice-based matter-wave interferometer (MWI) [31]. Such capability is made possible by being able to achieve large spatial separation of wave packets. Naively speaking, while a sequence of π pulses [32,33] can be used to spatially separate the wave packets, as illustrated in Fig. 1(c), pulse imperfections from Rabi frequency amplitude noise can both generate a large uncertainty and reduce the value of the achievable separation. These issues can be mitigated using adiabatic topological pumping schemes (detailed in Sec. V). As schematically illustrated in this panel, the spatial separation generated via adiabatic topological pumping methods can reach larger values with reduced uncertainty.

We emphasize that, given the noninteracting conditions in consideration, our protocols do not generate entanglement, and therefore do not reduce quantum noise. Instead, our protocols help reduce the *classical statistical noise* caused by relevant experimental imperfections, opening a path for state-of-the-art clocks operating at the desired SQL sensitivity.

More specifically, we study the performance of our quantum sensing protocols in the presence of experimentally relevant static noise, including laser amplitude noise and noise arising from atomic motion and thermal effects [34–36]. We use realistic parameters and approximations in our analysis.

The rest of this paper is organized as follows. First, we discuss a protocol capable of engineering the SSH (RM) model with tunable model parameters in tilted OLCs. Then, we discuss how to use clock spectroscopy to probe and characterize the different topological phases of the SSH model. Finally, we discuss how topology protects the system's sensitivity against unwanted noise in quantum sensing protocols of (1) an optical frequency and (2) a constant uniform acceleration.

Our work can be readily implemented in current experimental platforms [8,10] and paves ways to study topological phases of quantum matter in OLCs. More importantly, our work opens up a path to use topological protection to improve clock operations.

II. THE SU-SCHRIEFFER-HEEGER MODEL IN A TILTED OLC

In this section, we discuss our proposal to simulate the SSH (RM) model, a prototypical model featuring SPT phases, in a 1D tilted OLC. We then briefly review the key concepts of this model relevant for the rest of this paper.

We consider a tilted, 1D OLC with lattice spacing a_L and nearest-neighbor tunneling frequency J, loaded with a dilute array of atoms in such a way the system can be considered as noninteracting, as shown in Fig. 1(a). The atoms have mass M_a, and experience a uniform acceleration g_{acc} generated by a linear potential across the lattice. The eigenstates of this system are the Wannier-Stark (WS) states, $|l\rangle$ [8,37], centered at lattice site l and with eigenenergy $E_l = \hbar\Delta l$, where $\hbar\Delta \equiv M_a g_{\mathrm{acc}} a_L$ is the energy difference between atoms on adjacent lattice sites. We consider a parameter regime where the lattice depth is shallow enough that J is comparable to Δ, thus $|l\rangle$ is delocalized across several lattice sites. We show the WS states as shaded areas in the left panel of Fig. 1(a). The clock states correspond to two electronic levels, e and g, with an optical transition frequency ω_a. The single-particle Hamiltonian of our system

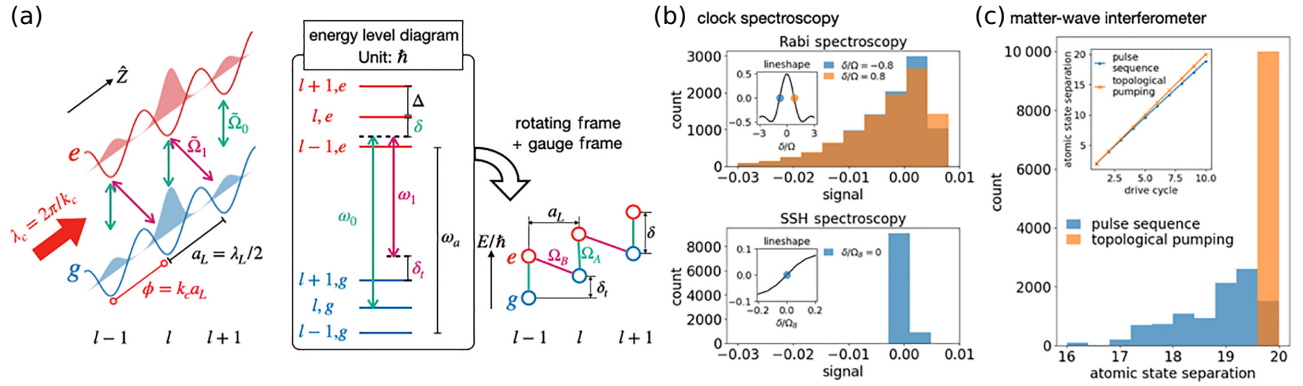

FIG. 1. A symmetry-protected topological OLC. (a) Simulating the SSH (RM) model in a tilted 1D OLC: by using two laser beams to drive both carrier and sideband transitions, a 1D Wannier-Stark ladder can be transformed into the SSH (RM) model that we use for quantum simulation and quantum sensing protocols discussed in the rest of the paper. Left panel: a schematic diagram of the experimental realization of $\hat{H}_{t\text{-RM}}$ in a tilted 1D OLC. We use a two-tone clock laser with wave vector k_c in a tilted 1D OLC with lattice constant a_L. When the clock laser is incommensurate with the optical lattice, atoms on neighboring lattice sites feel a spin-orbit-coupling phase $\phi = k_c a_L$. We show the Wannier-Stark wave functions as shaded red and blue areas. Center panel: the energy diagram relevant to generating the SSH (RM) model, as indicated in the right panel. (b),(c) Reducing undesirable noise via topologically robust protocols. Both panels include experimentally relevant, shot-to-shot noise (see also Secs. IV and V). Here we examine 100 realizations of global laser amplitude noise and 100 realizations local laser amplitude noise, assuming 0.1% global noise and 4% local noise, respectively. (b) Clock spectroscopy via Rabi (upper panel) and SSH (lower panel) protocols. The main panels show histograms of the signals at two opposite detunings as indicated in the legends and illustrated with the colored symbols in the insets. The insets in the upper and lower panels show the lineshapes of the corresponding protocols. (c) Spatial separation of the e and g atomic states in an OLC interferometer via a sequence of pulses (blue) and via an adiabatic, topological Thouless pumping scheme (orange). The main panels show the histograms of the atomic state separation after ten drive cycles. The inset shows the averaged spatial separation of the e and g states at a different number of cycles.

thus reads

$$\hat{H}^{\text{1p}}_{\text{lab}} = \hbar\Delta \sum_{l,\alpha=g,e} l\hat{\tilde{c}}^{\dagger}_{l\alpha}\hat{\tilde{c}}_{l\alpha} + \sum_{l} \hbar\omega_a \hat{\tilde{c}}^{\dagger}_{le}\hat{\tilde{c}}_{le}, \tag{1}$$

where $\hat{\tilde{c}}_{l\alpha}$ annihilates a fermionic particle in WS state $|l\rangle$ and electronic level $\alpha = g, e$. It is worth noting that the SSH (RM) model is a single-particle model, therefore independent of quantum statistics. However, in reality, Fermi statistics makes it easier to implement our protocol both by reducing the role played by interactions and for the initial state preparation.

We use a clock laser with wavelength λ_c, propagating along the lattice direction, to drive the ultranarrow clock transition $g - e$. When λ_c/a_L is not an integer value, the clock laser imprints a differential phase $\phi = k_c a_L$ across adjacent lattice sites, which generates the spin-orbit coupling (SOC) [30,38–40], allowing the clock laser to drive $g - e$ transitions between different sites. We propose to use two different clock laser tones to implement the SSH (RM) model. The first tone with angular frequency ω_0, detuned from the atomic transition by $\delta = \omega_0 - \omega_a$, drives the on-site ("carrier", $|l, g\rangle \to |l, e\rangle$) transition [see Fig. 1(a) and Appendix A for details]:

$$\hat{H}^{\tilde{\Omega}_0}_{\text{lab}} = \frac{\hbar\tilde{\Omega}_0}{2} e^{-\mathbf{i}\omega_0 t} \sum_{l} \hat{\tilde{c}}^{\dagger}_{le}\hat{\tilde{c}}_{lg} + \text{h.c.}, \tag{2}$$

where $\tilde{\Omega}_0 = \Omega^c \langle l|e^{\mathbf{i}k_c\hat{X}}|l\rangle \simeq \Omega^c I_0 \mathcal{J}_0(\tilde{J})$ with Ω^c the bare Rabi frequency of the carrier drive and $I_0 = \int dX e^{\mathbf{i}k_c X} w_0^2(X)$ the on-site overlapping integral of the localized ground-band Wannier function $w_0(X)$, and $\mathcal{J}_n(\tilde{J})$ the nth Bessel function of the first kind with $\tilde{J} = 4J\,|\sin(\phi/2)|\,/\Delta$. The second tone with angular frequency ω_1 is used to drive a "red sideband" transition, $|l, g\rangle \to |l-1, e\rangle$, with two-photon detuning $\delta_t = \omega_1 - \omega_0 + \Delta$. The Hamiltonian thus reads [see Fig. 1(a) and Appendix A for more details]:

$$\hat{H}^{\tilde{\Omega}_1}_{\text{lab}} = \frac{\hbar\tilde{\Omega}_1}{2} e^{-\mathbf{i}\omega_1 t} \sum_{l} \hat{\tilde{c}}^{\dagger}_{le}\hat{\tilde{c}}_{l+1g} + \text{h.c.}, \tag{3}$$

where $\tilde{\Omega}_1 = \Omega^s \langle l-1|e^{\mathbf{i}k_c\hat{X}}|l\rangle \simeq \mathbf{i}\Omega^s I_0 \mathcal{J}_{-1}(\tilde{J})$ and Ω^s is the bare Rabi frequency of the sideband drive. In the above equations, we removed the SOC phase via a gauge transformation: $\hat{\tilde{c}}^{\dagger}_{le} \to e^{-\mathbf{i}l\phi/2}\hat{\tilde{c}}^{\dagger}_{le}$, $\hat{\tilde{c}}^{\dagger}_{lg} \to e^{\mathbf{i}l\phi/2}\hat{\tilde{c}}^{\dagger}_{lg}$. When driving close to resonance of both transitions, it is convenient to go to a rotating-gauge frame (RGF) via

$$\hat{\tilde{c}}^{\dagger}_{le} \to \mathbf{i}^l\, e^{\mathbf{i}t[(\omega_0-\omega_1)l+\omega_0]}\hat{a}^{\dagger}_{le}, \quad \hat{\tilde{c}}^{\dagger}_{lg} \to \mathbf{i}^l\, e^{\mathbf{i}t(\omega_0-\omega_1)l}\hat{a}^{\dagger}_{lg}. \tag{4}$$

Under this unitary transformation we can identify fast-rotating terms, which can be removed since they average out. To avoid exciting the atoms to undesired state during laser interrogation, we assume $|\tilde{\Omega}_0|, |\tilde{\Omega}_1| \ll \Delta$. This leads

us to a tilted RM (t-RM) model:

$$\hat{H}_{t\text{-RM}}/\hbar = \hat{H}_{\text{RM}}/\hbar + \delta_t \sum_{l,\alpha=e/g} l\hat{a}^\dagger_{l\alpha}\hat{a}_{l\alpha}, \tag{5}$$

where

$$\hat{H}_{\text{RM}}/\hbar = \sum_l \left(\frac{\Omega_A}{2}\hat{a}^\dagger_{le}\hat{a}_{lg} + \frac{\Omega_B}{2}\hat{a}^\dagger_{le}\hat{a}_{l+1g} + \text{h.c.}\right) + \frac{\delta}{2}\sum_l \left(\hat{a}^\dagger_{lg}\hat{a}_{lg} - \hat{a}^\dagger_{le}\hat{a}_{le}\right), \tag{6}$$

with $\Omega_A = \tilde{\Omega}_0, \Omega_B = -\mathbf{i}\tilde{\Omega}_1$, both real valued. When both drives are on resonance ($\delta = \delta_t = 0$), we obtain the SSH model: $\hat{H}_{\text{SSH}}/\hbar = \sum_l \left(\Omega_A \hat{a}^\dagger_{le}\hat{a}_{lg} + \Omega_B \hat{a}^\dagger_{le}\hat{a}_{l+1g} + \text{h.c.}\right)/2$. At this leading order, we have ignored the ac Stark shifts generated by both lasers, see Appendix B for details. These terms contribute to undesired noise that we include in later sections.

A schematic visualization of the above protocol is shown in Fig. 1(a). All of the model parameters, namely, $\Omega_A, \Omega_B, \delta$, and δ_t can be tuned: δ and δ_t can be tuned via tuning laser frequencies as long as they are smaller than Δ; Ω_A and Ω_B can be tuned either by tuning the laser Rabi frequencies Ω^c and Ω^s, the lattice depth (which modifies I_0 and J), the spin-orbit coupling phase ϕ [41], or the tilting potential $\hbar\Delta$ [7].

The SSH (RM) model has two dimerized phases determined by $r \equiv |\Omega_B/\Omega_A|$. The transition between them is at $r = 1$, which sets the topological critical point for the SSH model. When $r < 1$, the SSH model is in the topologically trivial (T) phase, while when $r > 1$, the topologically nontrivial (NT) phase. One way to visualize these two phases is by rewriting the model in the quasimomentum (k) basis: $\hat{a}_{k\alpha} = (1/\sqrt{L})\sum_l e^{\mathbf{i}lka_L}\hat{a}_{l\alpha}$, which can then be used to define spin operators acting in quasimomentum space, $\hat{S}^+_k = \hat{a}^\dagger_{ke}\hat{a}_{kg}$ and $\hat{S}^z_k = (\hat{a}^\dagger_{ke}\hat{a}_{ke} - \hat{a}^\dagger_{kg}\hat{a}_{kg})/2$. The spin operators satisfy standard commutation relations. In this way, $\hat{H}_{\text{SSH}}$ can be written as a spin model

$$\hat{H}_{\text{SSH}} = \sum_k \vec{B}(k)\cdot\hat{\vec{S}}_k, \tag{7}$$

where $\hat{\vec{S}}_k = (\hat{S}^x_k, \hat{S}^y_k, \hat{S}^z_k)$, and the effective magnetic field is defined as $\vec{B}(k) \equiv (\Omega_A + \Omega_B\cos ka_L, \Omega_B \sin ka_L, 0) \equiv (|B|\cos(\phi_k), |B|\sin(\phi_k), 0)$, where ϕ_k is the angle between $\vec{B}(k)$ and the x axis in the $x-y$ plane of the Bloch sphere. The topology of the SSH model can thus be seen through a closed trajectory of $\vec{B}$ along the Brillouin zone (BZ), $ka_L \in (-\pi, \pi]$. As shown in Fig. 2, the T/NT phase depends on whether or not this trajectory winds around the origin, as defined by the "winding number" $\mathcal{W}$ or the Zak phase $\phi_{\text{Zak}} = -\pi\mathcal{W}$. Mathematically, for the SSH model, $\mathcal{W}_{\text{SSH}} = -(1/\pi)\int_{\text{BZ}} \mathcal{A}(k)\,dk$ with the Berry phase $\mathcal{A}(k) = -\frac{1}{2}\,d\phi_k/dk$, resulting in $\mathcal{W}_{\text{SSH}} = 0$ when $r < 1$ and $\mathcal{W}_{\text{SSH}} = 1$ when $r > 1$.

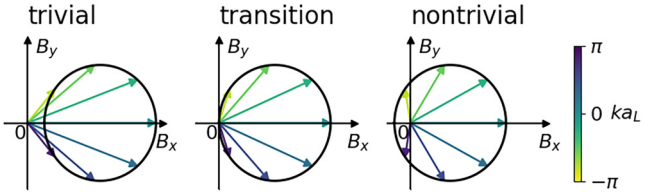

FIG. 2. Schematic illustration of the winding number of the SSH model. In all panels, the arrows display the effective magnetic field of the SSH model, $\vec{B}(k)$, as ka_L varies over the BZ. Different colors represent different values of k. When $r < 1$ (left), the winding number is zero and the system is topologically trivial. At $r = 1$ the system reaches a critical point (center), and for $r > 1$ (right) there is a net finite winding number thus a nontrivial topology. Black circles indicate the trajectories traced by the tip of $\vec{B}(k)$ as k varies across the BZ.

A nontrivial Berry phase can give rise to topological Thouless pumping [42,43] when one varies the RM model parameters (Ω_A, Ω_B, and δ) in a way that they adiabatically return to their initial values after a pump cycle time τ. We discussed this in the latter part of this paper, Sec. V and in particular, in Fig. 6 and corresponding discussions. The particle transport at the end of each cycle is restricted to be an integer number set by $\mathcal{W}$ as the trajectory of $(\delta, \Omega_A - \Omega_B)$ winds around the origin once, otherwise there is no particle transport. The direction towards which the particle moves is determined by its initial state and the winding direction of $(\delta, \Omega_A - \Omega_B)$. The topological Thouless pumping has been shown to be robust against weak perturbations including certain interactions, time-independent spatial disorder and time-dependent disorder [12,19,43–45].

III. A SPECTROSCOPIC PROBE OF THE TOPOLOGICAL PHASE TRANSITION

In the following section, we discuss how we can use standard clock spectroscopy to probe $\mathcal{W}_{\text{SSH}}$, the topological nature of the SPT phases in our system, either when $\delta = \delta_t = 0$, or when $\delta_t = 0$ with fixed δ.

We use the states $\{|\downarrow\rangle_l \equiv |l+1, g\rangle, |\uparrow\rangle_l \equiv |l, e\rangle\}$ as an effective two-level system to perform the read out, as done in prior work [6,8]. In terms of these states, we can define the corresponding sideband spin-1/2 operators: $\hat{I}_{ly} \equiv (\hat{a}^\dagger_{le}\hat{a}_{l+1g} - \hat{a}^\dagger_{l+1g}\hat{a}_{le})/(2\mathbf{i})$, $\hat{I}_{lx} \equiv (\hat{a}^\dagger_{le}\hat{a}_{l+1g} + \hat{a}^\dagger_{l+1g}\hat{a}_{le})/2$ and $\hat{I}_{lz} \equiv (\hat{a}^\dagger_{le}\hat{a}_{le} - \hat{a}^\dagger_{l+1g}\hat{a}_{l+1g})/2$, which satisfy the appropriate commutation relations. In a typical clock measurement, one measures the *global* observables given by the sum of all local observables, namely $\hat{O} = \sum_l \hat{O}_l$. We also simplify the expectation value of an operator as $O =$

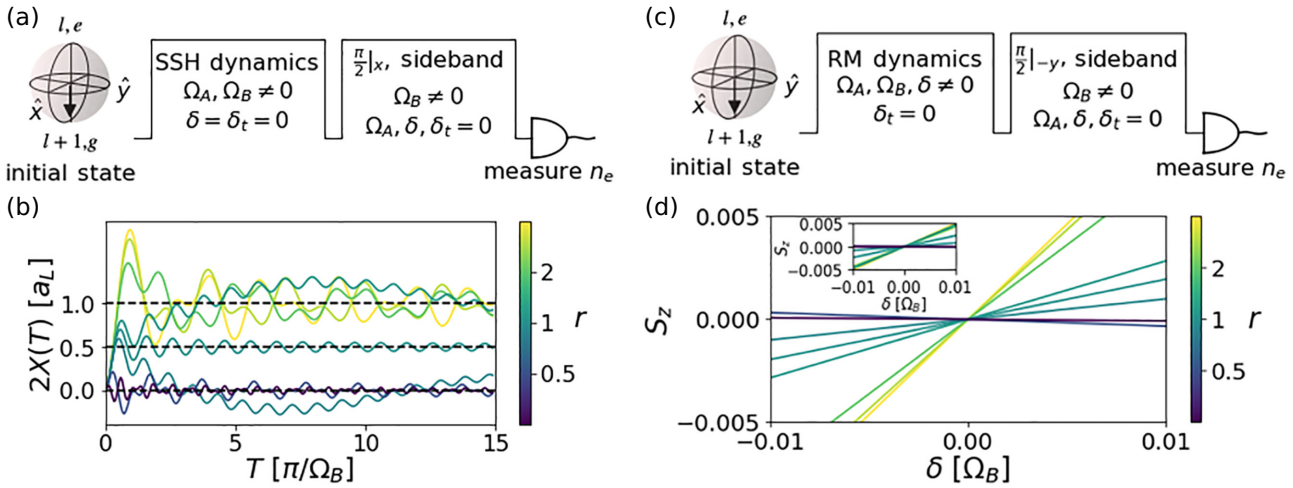

FIG. 3. Probing topological phases in the SSH model. (a),(c) Protocols in the rotating-gauge frame. (b),(d) Numerical simulations. (a),(b) Winding number measurements with $\delta = \delta_t = 0$, compared to their expected values (0, 0.5, and 1, shown as black horizontal dashed lines) in their corresponding topological phases. Line colors correspond to different r values indicated by the colorbar. (c),(d) One-step winding number measurements with $\delta \neq 0$ and $\delta_t = 0$. (d) One-step measurement results as a function of δ at $\Omega_B t = \pi$ (main panel) and $\Omega_B t = 15\pi$ (inset). At long time, the slope at $\delta = 0$ gives half of the winding number value. The main panel and the inset share the same x and y axis, with parameters: $\delta/\Omega_B = -0.1 \cdots 0.1$, $r = 0.3 \cdots 3$, and $\delta_t = 0$.

$\langle \hat{O} \rangle$. Additionally, since $\hat{I}_z$ is the global particle number difference between e and g states, $\hat{I}_z = \hat{S}_z \equiv \sum_l (\hat{n}_{le} - \hat{n}_{lg})/2$, where $\hat{n}_{l,e/g} = \hat{a}^\dagger_{l,e/g} \hat{a}_{l,e/g}$.

We sketch the schematics of the $\mathcal{W}_{\mathrm{SSH}}$ measurement protocol in Fig. 3(a): first, we prepare the atoms in the g internal level, each in a Wannier-Stark eigenstate. Similar to Rabi spectroscopy, we illuminate the atoms for time t. However, in our case, to implement the SSH model, we turn both laser tones on, and drive the carrier and sideband transitions *simultaneously* on resonance, namely, $\delta = \delta_t = 0$. At the end of the time evolution, instead of measuring the excitation fraction directly, we need to measure the total sideband coherence, I_y, along a quadrature perpendicular to the already-applied sideband tone. The latter can be measured by suddenly turning off the carrier drive while keeping the sideband drive on, for the specific time required to drive a sideband $\pi/2$ pulse, $U^{m_1}_{\mathrm{RGF}} = \exp[-\mathbf{i}(\pi/2)(\sum_l \hat{I}_{lx})]$, followed by measuring total excited- and ground-state populations $n_{e/g} \equiv \langle \hat{n}_{e/g} \rangle = \sum_l \langle \hat{n}_{l,e/g} \rangle$ to obtain S_z.

By measuring the sideband coherence I_y, we can in fact measure the current in the SSH chain given by the rate of change of the wave-function displacement:

$$\frac{\dot{\hat{X}}}{a_L} = \Omega_B \hat{I}_y, \tag{8}$$

where the displacement is $\hat{X} = a_L \sum_l l(\hat{n}_{le} + \hat{n}_{lg})$. A similar protocol was performed in quantum gas microscopes to measure currents with single-site resolution [46].

To probe the topological phase transition, one has to repeat this protocol and measure $I_y(t)$ at different time t to obtain its time integral. When weighted by Ω_B, we obtain the displacement of the atomic wave function from its initial location, $X(T)$:

$$\frac{X(T)}{a_L} = \Omega_B \int_0^T dt\, I_y(t). \tag{9}$$

We show in Fig. 3(b) that $X(T)$ can be used to probe topological phases of the SSH model, i.e.,

$$\frac{X(T)}{a_L} = \frac{\mathcal{W}_{\mathrm{SSH}}}{2} + \text{oscillating terms}. \tag{10}$$

In fact, the quantity $X(T)$ is equivalent to the "mean displacement"(MD), a bulk observable that can be used as a marker of topological phases [47–49]. The MD has been used to measure winding numbers in twisted photons [48], and can be used to study the topological properties of more complicated models [49].

The simple limiting cases when the system is totally dimerized, with $\Omega_B \neq 0, \Omega_A = 0$ and $\Omega_A \neq 0, \Omega_B = 0$, can serve to illustrate the distinct behaviors in the two different topological phases. In the former case, the NT phase, the atom performs standard Rabi oscillations in the sideband transition $I_y(t) = \sin(\Omega_B t)/2$ and therefore $X(T)/a_L = (1 - \cos(\Omega_B T))/2$; while in the latter case, the T phase, only the carrier transition is driven, thus atoms remain localized at their initial sites and thus $I_y(t) = X(T) = 0$.

In the presence of a small detuning, δ, from the carrier transition, we can measure the MD in *one step*, without integrating over time, by measuring the x component of the sideband coherence I_x after time evolution. We measure I_x by suddenly applying a phase jump of $-\pi/2$ to the Rabi sideband drive while simultaneously turning off the carrier Rabi drive, for a time necessary to realize a $\pi/2$ pulse, $U_{\mathrm{RGF}}^{m_2} = \exp\left[\mathbf{i}(\pi/2)(\sum_l \hat{I}_{ly})\right]$, followed by a measurement of the excited- and ground-state populations $n_{e,g}$. We display the above protocol in Fig. 3(c). One can show analytically using linear responses that when $\delta_t, \delta \ll \Omega_A, \Omega_B$,

$$I_x(t) \simeq \frac{\delta}{\Omega_B}\frac{\mathcal{W}_{\mathrm{SSH}}}{2} + \delta_t \tilde{S}(\Omega_A, \Omega_B) + \text{osc. terms}, \qquad (11)$$

where $\tilde{S}(\Omega_A, \Omega_B)$ is a real-valued function not directly related to $\mathcal{W}_{\mathrm{SSH}}$ (see Appendix D and Fig. 8 for details). The above equation indicates that the kinetic term I_x [46] responds linearly to the inversion-symmetry-breaking terms δ and δ_t, with a slope related to $\mathcal{W}_{\mathrm{SSH}}$ for the carrier detuning δ. Again, in the simple limiting case when the system is fully dimerized, we see that $I_x(t) = 0$ when $\Omega_A \neq 0,\ \Omega_B = 0$, while $I_x(t) \simeq (\delta + \delta_t)(1 - \cos(\Omega_B t))/2$ when $\Omega_A = 0,\ \Omega_B \neq 0$.

We show the numerical simulations of $I_x(t)$ with $\delta_t = 0$, at $t = \pi/\Omega_B$ and $t = 15\pi/\Omega_B$ in Fig. 3(d) and its inset. This provides us a one-step measurement of $\mathcal{W}_{\mathrm{SSH}}$: as long as we know the values of Ω_B and δ, we can measure $\mathcal{W}_{\mathrm{SSH}}$ via I_x. In fact, I_x is a band correlation function discussed in prior work [45], and has been found to be robust to certain types of disorder.

The same quantity can alternatively be measured by first preparing an initial state $(|0, g\rangle + |-1, e\rangle)/\sqrt{2}$, then turning on the RM dynamics for time t, followed by measuring $-S_z$. We show this protocol in Appendix E. Mathematically, this protocol is equivalent to the protocol discussed above.

It is worth noting that Eq. (11) assumes an infinite number of lattice sites with periodic boundary conditions. In Appendix F, we discuss how finite-size effects and open boundary conditions modify $I_x(t = 15\pi/\Omega_B)$ and affect the sharpness of the phase transition. We also discuss the robustness of $I_x(t = 15\pi/\Omega_B)$ to various levels of static, shot-to-shot amplitude uncertainties of Ω_A and Ω_B in finite chains.

IV. SSH CLOCK SPECTROSCOPY

We now discuss a clock spectroscopy protocol that is robust against unwanted noise in laser parameters thanks to the underlying topology of the system. We focus on time-independent global and local amplitude laser noise. The global amplitude noise is modeled as global variations of the Rabi frequency. On the other hand, the local amplitude noise is modeled as position-dependent Rabi frequency variations felt by each atom as it spreads over the radial direction of the OLC due to their finite radial temperature [35,36]. We do not include global laser phase noise in our analysis, because clock spectroscopy is inherently sensitive to it and thus such noise is always detrimental. Additionally, The SSH model is not immune to such noise as it breaks the symmetry of the model (i.e., the "Chiral symmetry").

In conventional Rabi spectroscopy, the atomic frequency is inferred via the so-called Rabi lineshape [illustrated in the inset of the upper panel of Fig. 1(b)], obtained by first driving a carrier laser with Rabi frequency Ω_R for a time t_R such that $\Omega_R t_\pi^R = \pi$, with the laser frequency detuned from the clock transition frequency by a detuning δ, followed by measuring populations n_e, n_g as a function of δ. The resonance value $\omega_a = \omega_0$ is given by the solution of $(n_e^{-1}(\delta_c) + n_e^{-1}(\delta_c'))/2 = \delta_{\mathrm{resonance}} = 0$, typically by choosing δ_c and δ_c' at the positive and negative slopes of the Rabi line shape at half maximum (FWHM), namely, where the line shape achieves maximum positive and negative slopes. Uncertainties in Ω_R lead to an uncertainty of t_π^R that in turn induces both a systematic error on the inferred resonant detuning at the FWHM, as well as a reduction of the signal at $\pm\delta_c$.

Our SSH clock spectroscopy adopts a similar idea as the Rabi spectroscopy, but we determine ω_a using the winding number measurement protocol, I_x, as discussed in Sec. III and Figs. 3(c) and 3(d). Specifically, we operate in the NT phase by setting $\Omega_B > \Omega_A$, let the system evolve for a fixed time $t_\pi^B = 5\pi/\Omega_B$ when the value of I_x saturates around $\mathcal{W}/2$, then measure I_x.

In addition to the carrier detuning, however, in our symmetry-protected SSH clock, there is also an additional detuning δ_t. In Fig. 4(a) we show that I_x varies linearly with respect to δ and δ_t, as discussed in Eq. (11). The relevant bare parameters, ω_a and Δ, are inferred by finding a set of detunings that satisfy $I_x(\delta, \delta_t) + I_x(-\delta, -\delta_t) = 0$. To measure clock transition frequency, we set $\delta_t = 0$, in which case the frequency difference between the two laser tones is Δ.

In the presence of the noise discussed above, the SSH Hamiltonian becomes $\hat{H}_{\mathrm{SSH}}/\hbar = \sum_{il}\left(\Omega_{iA}\hat{a}_{ile}^\dagger \hat{a}_{ilg} + \Omega_{iB}\hat{a}_{ile}^\dagger \hat{a}_{il+1g} + \mathrm{h.c.}\right)/2$, where the Rabi frequencies applied to each atom i is

$$\Omega_{i,A/B} = \bar{\Omega}_{A/B}\,(1 + \epsilon_a)\,(1 + \epsilon_i)\,, \qquad (12)$$

with $\bar{\Omega}_{A/B}$ the ideal value, ϵ_a the shot-to-shot global amplitude noise, and ϵ_i the local amplitude noise. We take ϵ_a and ϵ_i to be zero-mean Gaussian random variables with standard deviation σ_a and σ_i, respectively. We also include the additional ac Stark shifts (see Appendix B). In our simulation, we use current experimentally relevant values and set

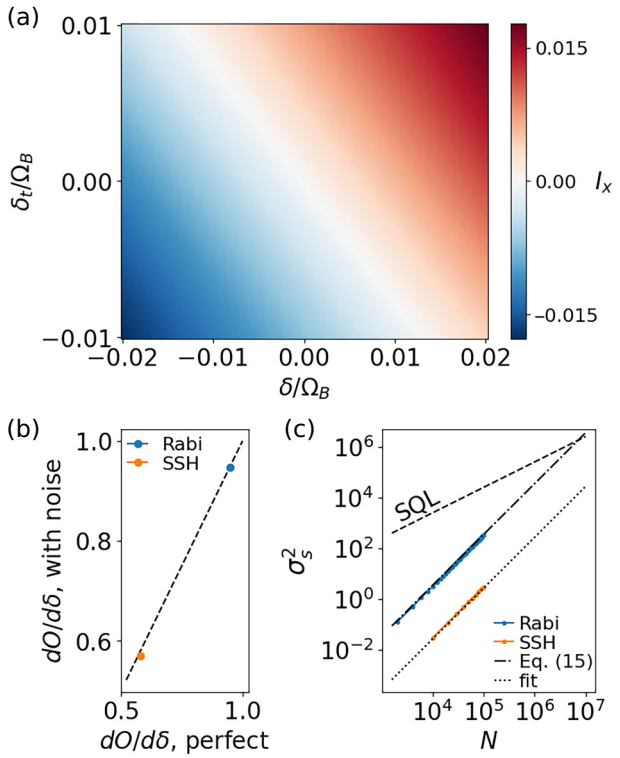

FIG. 4. (a) The signal of the SSH spectroscopy, I_x, at different δ and δ_t values without any experimental imperfections. (b),(c) Comparisons between Rabi spectroscopy (in blue) and SSH spectroscopy (in orange) with $\Omega_A/(2.2\pi) = \Omega_B/(2\pi) = 10\,\mathrm{Hz}$, over 200 realizations of global noise and N atom-dependent noise as detailed in the the main text. (b) How signal varies with respect to δ, $dO/d\delta$, at operation points δ_c's of the two protocols. For Rabi spectroscopy, $O = S_z$ and $\delta_c \sim 0.8\Omega$; for SSH spectroscopy, $O = I_x$ and $\delta_c = 0$, averaged over all noise realizations. (c) N dependence of σ_s^2 of the two protocols. The dashed line shows the fundamental sensitivity achievable for uncorrelated atoms, the SQL. The dashed-dotted line compares Rabi results to Eq. (15). The dotted line is a fit to the SSH results, which is $y = \gamma^2\sigma_a^2 N^2$, where $\gamma^2 = 0.00027$.

$\sigma_a = 0.001$ and $\sigma_a = 0.04$ [34–36]. We also set the Rabi frequencies to be $\Omega_B/(2\pi) = 10\,\mathrm{Hz}$ and $\Omega_A = \Omega_B/1.1$.

We compare the signals of the two protocols, i.e., $dO/d\delta$ with $O = S_z$ for Rabi and $O = I_x$ for SSH, at their respective operation points δ_c, with $\Omega_R = \Omega_B$. We observe minimal signal reductions in both protocols as shown in Fig. 4(b).

To quantify the robustness of a measurement protocol against imperfections, we calculate the clock sensitivity to δ, for a system of N noninteracting atoms as

$$\Delta^2\delta = \left.\frac{\overline{\Delta^2 O}}{t_L^2(dO/d\varphi)^2}\right|_{\delta\to\delta_c}, \quad \overline{\Delta^2 O} = N/4 + \sigma_s^2, \tag{13}$$

where t_L is the laser interrogation time, φ is the accumulated phase due to δ, δ_c is the working point of the noise-free protocol, O is the measured observable which gives the signal, and associated variance $\overline{\Delta^2 O}$. The variance includes both the quantum noise, or SQL, of $N/4$ for noninteracting atoms, and the statistical noise σ_s^2, coming from the sensitivity of a protocol to technical noise. For the collective observable measured in the described protocols, $O = S_z$, the global noise increases quadratically in N [50,51], namely,

$$\sigma_{s,\mathrm{gl}}^2 \simeq \sum_\beta \sigma_{\Omega_\beta,\mathrm{gl}}^2 \underbrace{\sum_{i\neq j}\left(\left.\frac{\partial O_i}{\partial\Omega_\beta}\right|_{\bar\Omega_\beta}\right)\left(\left.\frac{\partial O_j}{\partial\Omega_\beta}\right|_{\bar\Omega_\beta}\right)}_{\propto N^2}, \tag{14}$$

where gl stands for global, β is all the Rabi frequencies involved in the protocol, i.e., $\beta = R$ for the Rabi spectroscopy and $\beta = A, B$ for the SSH spectroscopy, and $O_{i/j}$ is the measured observable of atom i/j. For Rabi spectroscopy, it can be analytically calculated that

$$\sigma_{s,\mathrm{gl}}^2 \simeq 0.035 N^2 \sigma_{\Omega_R,\mathrm{gl}}^2. \tag{15}$$

The noise affecting individual atoms, on the other hand, scales linearly in N, and is suppressed when N is large.

In the case of the SSH spectroscopy, σ_s^2 is suppressed since $\partial I_{ix}/\partial\Omega_\beta$ is small, as $I_{ix} \propto \mathcal{W}_{\mathrm{SSH}}\delta$ where $\mathcal{W}_{\mathrm{SSH}}$ is topologically protected against static amplitude uncertainties of $\Omega_{A,B}$ [21,45]. We discuss this briefly in Appendix F.

We compare σ_s^2 of our protocol with that of the Rabi spectroscopy in Fig. 4(c) as a function of total particle number N, assuming perfect I_x measurements. We observe a reduction of σ_s^2 in the SSH spectroscopy. By fitting σ_s^2 at different N values to $y = \gamma^2\sigma^2 N^2$, we obtain $\gamma^2 \simeq 0.00027$. We also compare our simulation with the SQL shown by the black dashed line in Fig. 4(c) and compare σ_s^2 of the Rabi spectroscopy to Eq. (15). Given the small Rabi frequency noise we consider, σ_s^2 of the Rabi spectroscopy becomes comparable with the SQL only for $N \gtrsim 10^7$. That means that while not so relevant under current conditions, the discussed SSH protocol could be beneficial to future generation OLCs capable of interrogating larger atom arrays. Other types of local amplitude noise ignored here could push the utility of our protocol even to lower N.

If it is not possible to measure I_x perfectly, the same quantity can alternatively be measured using the protocol mentioned in the end of the last section, or in Appendix E, where the initial state can be prepared adiabatically, and S_z can be measured fairly accurately.

V. TOPOLOGICALLY PUMPED MATTER-WAVE INTERFEROMETER

Conventional interferometers detect force fields, such as the ones proportional to the local gravitational acceleration g [52] and the Newtonian gravitational constant G [53], via

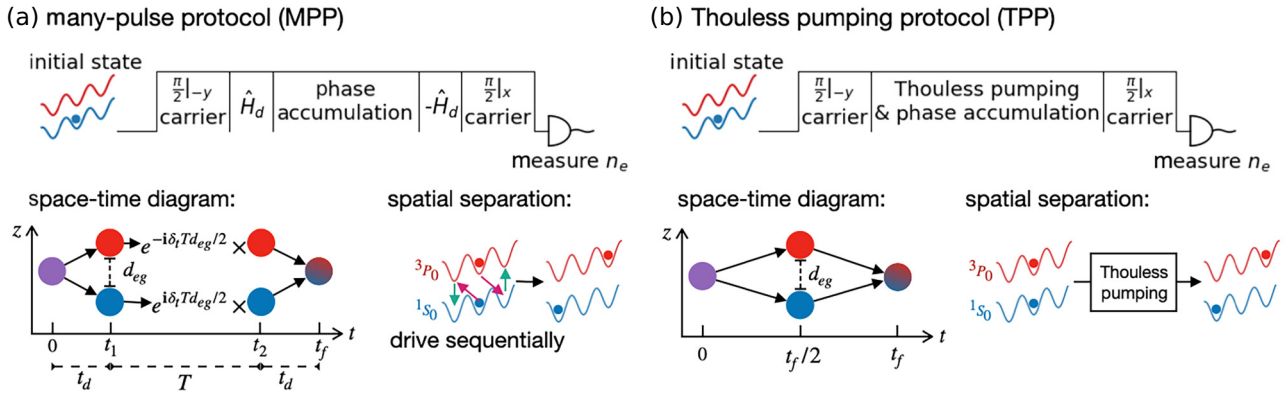

FIG. 5. MWIs in OLCs. (a) The "many-pulse protocol" (MPP). (b) The "Thouless pumping protocol" (TPP). Upper panels: the protocol sequence of each protocol as described in the main text. Lower left panels: the space-time diagram of each protocol. Lower right panels: pictorial indication of one drive cycle of each protocol that creates $d_{eg} = 2a_L$.

measuring the differential phase, φ, experienced by matter waves traveling through different paths in the force field. These MWIs typically operate using free-falling atoms that enjoy a phase accumulation that scales quadratic in time [52]. While trapping the atoms in optical lattices [31,54–58] has the advantage of a much longer interrogation time, currently approaching minutes, the achievable phase-accumulation rate is limited to scaling linearly with time. A way to further enhance the accumulated phase is via the application of multiple pulses [32,59] that helps to increase the spatial separation between the two parts of the wave packet.

In a possible implementation of the protocol [32,33], one first applies an initial carrier $\pi/2$ pulse on atoms prepared in their ground state, generating a coherent superposition on a single site l: $|\psi_0^{MWI}\rangle = (|l,g\rangle + |l,e\rangle)/\sqrt{2}$. Then, for a duration t_d, a sequence of N_p^M composite π pulses, consisting of a sideband drive followed by a carrier drive, denoted as $\hat{H}_d$, is applied to induce a spatial separation between $|e\rangle$ and $|g\rangle$ states: $d_{eg} = 2N_p^M a_L$. Afterwards, within a dark time $T \gg t_d$, the two states accumulate a differential phase since they are spatially separated at locations with different gravitational potential. Then, after a pulse sequence that reverses the spatial separation, denoted as $-\hat{H}_d$, the atoms are recombined. Lastly, we measure the accumulated phase difference by applying another local carrier $\pi/2$ pulse that converts the y component of the carrier coherence into population, which is the quantity measured at the end of the sequence. Assuming fast and perfect $\pi/2$ pulses for the state preparation and measurement, the total time of this protocol is $t_f = 2t_d + T$. This MWI signal depends linearly on the accumulated phase. We refer to this protocol as the "many-pulse" protocol (MPP), and illustrate it in Fig. 5(a). Assuming perfect drives with $\delta = 0$, the ideal accumulated phase of the MPP is

$$\varphi^M_{\text{ideal}} = \delta_t T d_{eg}/a_L = 2\delta_t(t_f - 2t_d)N_p^M. \tag{16}$$

We now discuss an alternative MWI protocol that shows reduced sensitivity of unwanted noise thanks to the use of topologically protected adiabatic transfer instead of a multipulse sequence. The basic idea is to achieve the desired spatial separation using the topological "Thouless pumping" protocol (TPP), shown in Fig. 5(b). In this case, within the same time duration t_f , half of the time is spent to repeat N_p^T Thouless pumping cycles with a cycle time τ, in order to spatially separate the $|g\rangle$ and $|e\rangle$ states by $d_{eg} = 2N_p^T a_L$. Then, the same amount of time is used to bring the two states back to the initial location, and measure the accumulated phase in the same way as in the MPP. No dark time is needed in this protocol as the two states continuously accumulate differential phase during the adiabatic Thouless pumping cycles. We sketch in Fig. 6(a) the time variation of the RM parameters (left panel) used to perform a pumping cycle with duration $\tau = 1/12$ s and their corresponding laser frequencies (right panel): in the protocol, we vary ω_1 together with ω_0, so that the value of δ_t is kept at a fixed value at all time. In the left panel of Fig. 6(b), we show the spatial distribution of the states e and g in the lattice, $n_{l,e/g}$, during two Thouless pumping cycles. We also show in the right panel of Fig. 6(b) the time dependence of $(\delta,\ \Omega_A - \Omega_B)$ within one Thouless pumping cycle.

Contrary to the MPP, the ideal accumulated phase scales *quadratically* with t_f, which is also the case for free-falling atoms:

$$\varphi^T_{\text{ideal}} = 4\delta_t \sum_{n=0}^{N_p^T}(n\tau) = 2\delta_t\tau\left(N_p^T\right)^2 = \delta_t t_f^2/(2\tau). \tag{17}$$

We compare the MPPs and TPP performance with fixed $t_f = 4s$ and $\varphi^M_{\text{ideal}} = \varphi^T_{\text{ideal}}$. In particular, we consider three different MPPs, i.e., protocols P_0 to P_2 with $\Omega_A = \Omega_B = \Omega$, where P_0: $\Omega/(2\pi) = 24$ Hz, $N_p^M = 24$, $T = 2$ s; P_1: $\Omega/(2\pi) = 37.5$ Hz, $N_p^M = 15$, $T = 3.2$ s; and P_2: $\Omega/(2\pi) = 39.86$ Hz, $N_p^M = 65$, $T \simeq 0.74$ s, adjusting the

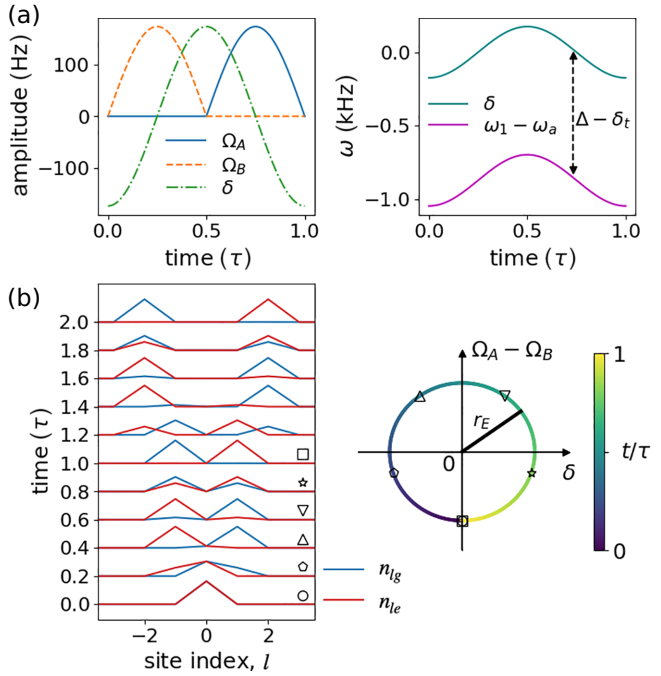

FIG. 6. Thouless pumping in a tilted 1D OLC. (a) Time dependence of the Hamiltonian parameters Ω_A, Ω_B, and δ (left panel) and laser frequencies (right panel) of one Thouless pumping cycle of time $\tau = 1/12$ s. (b) Left panel: the dynamics of the probability density function of the e (red) and g (blue) states of an atom within two Thouless pumping cycle, with initial state: $(|0,g\rangle + |0,e\rangle)/\sqrt{2}$. Right panel: time dependence of $(\delta, \Omega_A - \Omega_B)$ of one Thouless pumping cycle, with time indicated by the colormap. The radius, r_E, which gives the band gap as $L \to \infty$, is constant in t. Open symbols on the left panel corresponds to the time and Hamiltonian parameters shown on the right panel. Note that the first symbol (open circle) and the last symbol (open square) are on top of each other, indicating the time periodicity of Thouless pumping cycles.

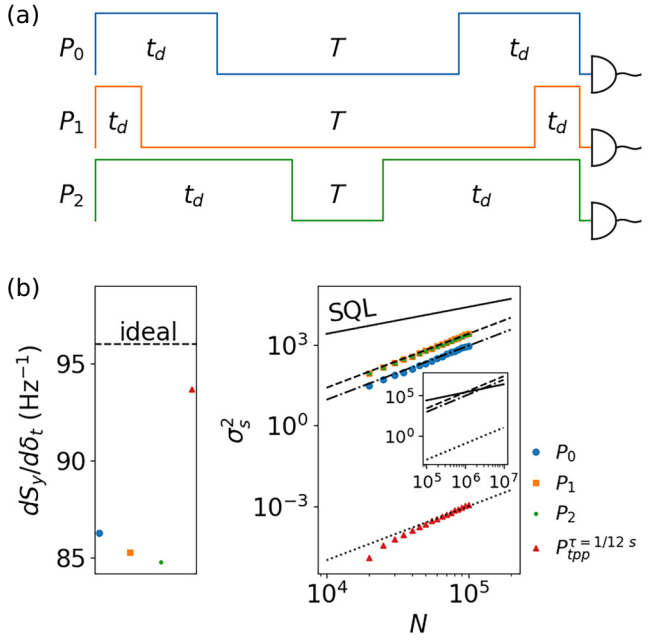

FIG. 7. Comparisons between the MPPs and TPP with 200 realizations of global imperfections and N noninteracting atoms with atom-dependent imperfections, as discussed in the the main text. (a) Pulse sequences of the MPP protocols $P_{0...2}$. (b) Left panel: how the signal S_y varies with respect to the detuning δ_t for the various protocols (symbols) compared to the ideal value (the black dashed line). Right panel: N dependence of σ_s^2 (symbols), compared with the SQL (black solid line). Black dashed, dashed-dotted, and dotted lines: fitting the symbols to $y = \gamma^2 \sigma_a^2 N^2$, where $\gamma^2 \simeq 0.25$ (dashed), $\gamma^2 \simeq 0.09$ (dashed-dotted) and $\gamma^2 \simeq 10^{-7}$ (dotted). The inset of the right panel shows the lines of the main panel, extrapolated to larger N values. It shows that for large $N > 3 \times 10^6$, the MPPs reach noise levels comparable with the SQL.

laser power to achieve the same Rabi frequency Ω for both the carrier and the sideband drives. These three chosen protocols aim to capture different ways to improve the MWI sequence by maximizing phase accumulations, although by no means they are the optimal ones: P_1 has long dark time T, and P_2 has long t_d thus leads to large d_{eg}, while P_0 balances t_d and T. We consider one TPP with $\tau = 1/12$ s and $N_p^T = 24$ (protocol $P_{\text{TPP}}^{\tau=1/12\,\text{s}}$). All of the protocols are designed to achieve the same phase accumulation under ideal conditions.

To investigate the robustness of these protocols, we account for relevant sources of noise, described by the function $\Omega_{i,A/B} = \bar{\Omega}_{A/B}(1+\epsilon_a)(1+\epsilon_i)$, the same as the previous section. We also include ac Stark shifts as discussed in Appendix B. The time dependence of δ in TPP thus becomes $\delta(t) = \delta_p(t) + \bar{\delta}_{\text{ACS}}(t) + \delta_{\text{ACS}}^{\epsilon}(t)$, where $\delta_p(t)$ is the actual detuning of the laser frequency ω_0 from the atomic transition frequency ω_a, which we vary over time during the protocol. The quantity $\bar{\delta}_{\text{ACS}}(t)$ is the ideal ac Stark shifts that can be calculated based on the instantaneous Rabi frequencies and Δ. In the presence of noise in Rabi frequency amplitudes, $\delta(t)$ has a time-dependent noise given by $\delta_{\text{ACS}}^{\epsilon} = \delta_{\text{ACS}}(t) - \bar{\delta}_{\text{ACS}}(t) \neq 0$.

We investigate the signals obtained for all the protocols and how they change with δ_t, i.e., $dS_y/d\delta_t$. Ideally, these protocols should have the same $dS_y/d\delta_t$ value. However, in the left panel of Fig. 7(b), we observe a reduction in all protocols due to experimental imperfections. Due to the imposed time constraint we also see a possible lack of full adiabaticity in the TPP protocol. Nevertheless, the TPP still appears to have the largest signal. We would like to note that the lack of full adiabaticity can be resolved by increasing τ and/or the maximum values of $|\Omega_{A/B}|$, by optimizing the pulse sequence, or via shortcuts-to-adiabaticity protocols [60]. It is worth noting that for topological pumping schemes, the particle transport is protected even in the presence of small interactions, as long as the interaction

strength is small compared to the energy gap of the SSH model [19,44].

Lastly, we compare the statistical noise of these protocols. As shown in the right panel of Fig. 7(b), the TPP yields significantly less statistical noise than the MPPs. We also compare all protocols with the SQL and find that the statistical noise of the MPPs is comparable with the SQL when $N > 3 \times 10^6$, while that of the TPP still remains much smaller than the SQL.

VI. CONCLUSION AND OUTLOOK

In this paper, we described a readily implementable experimental setting to realize a symmetry-protected topological model in a tilted 1D OLC. We discussed how one can measure the system's topological property, namely the winding number, by taking advantage of the pristine quantum coherence and the exquisite spectral resolution offered by OLCs. We finally discussed two sensing protocols, which showed robust sensitivity compared to conventional clock sequences, thanks to the topological robustness of symmetry-protected states against unwanted global and local noise present in real experiments. We discussed how topology helps reducing statistical uncertainties, while keeping or even increasing the acquired signal.

Our work can open up a new path for a generation of OLCs with topologically enhanced sensitivity. While we focused here on measuring the clock transition frequency ω_a and the local gravitational acceleration g, our protocols can, in principle, be adapted to improve the measurement resolution of gravitational red shifts [6]. Moreover, even though so far we have limited our analysis to noninteracting atoms, an exciting extension is to study how interactions affect the observed topological robustness [19,61]. Additionally, even though we focused our work on static imperfections, our protocols could, in principle, be robust against certain types of time-dependent noise [5,62]. Finally, generalizing the investigation to more complex systems including higher-dimensional models or systems with more than two internal levels, by incorporating the nuclear spins, will open up a plethora of rich physics, where for the first time the cooperation or competition between interactions and topology can give rise to a new generation of quantum-enhanced and topologically protected sensors.

ACKNOWLEDGMENTS

We thank Joanna Lis and Maya Miklos for feedback on the paper. We also thank Thomas Bilitewski, Mikhail Mamaev, Klaus Mølmer, Bhuvanesh Sundar, Yanqi Wang, and Haoqing Zhang for useful discussions. We additionally thank Jim McKown, Corey Keasling, and Daniel Packman from JILA computing group for their support with relevant hardware used for numerical simulations. This material is based upon work supported by the AFOSR FA9550-24-1-0179, the SLOAN, the Simons and the Heising-Simons foundations, the NSF JILA-PFC PHY-2317149 and OMA-2016244 (QLCI), the U.S. Department of Energy, Office of Science, National Quantum Information Science Research Centers, Quantum Systems Accelerator and NIST. T.E. also acknowledges funding from Swiss National Science Foundation under Advanced Grant No. TMAG-2 209376.

DATA AVAILABILITY

No data were created or analyzed in this study.

APPENDIX A: THE SSH MODEL IN A TILTED OLC

The Hamiltonian that describes the dynamics of atoms driven by a coherent laser, with Rabi frequency Ω, laser frequency ω_l, and wave number k_c, is given by

$$\hat{H}^{\Omega}_{\rm lab}/\hbar = \frac{\Omega}{2} e^{-\mathbf{i}\omega_l t} \int dX\, e^{\mathbf{i}k_c X} \hat{\Psi}^{\dagger}_e(X) \hat{\Psi}_g(X). \tag{A1}$$

Assuming the atoms are trapped in the lowest band of a lattice, we can expand the field operator in term of lowest band Wannier states localized at the different lattice sites, the above equation can be rewritten as $\hat{\Psi}_\alpha = \sum_n w_0(X - na_L)\hat{c}_{n\alpha}$, where a_L is the lattice constant. We thus get

$$\hat{H}_{\rm lab} = \frac{\Omega}{2} e^{-\mathbf{i}\omega_l t} \sum_{mn} I_{nm} \hat{c}^{\dagger}_{ne} \hat{c}_{mg}, \tag{A2}$$

where

$$I_{nm} = \int dX\, e^{\mathbf{i}k_c X} w_0(X - na_L) w_0(X - ma_L) = e^{\mathbf{i}n\phi} I_{m-n}, \tag{A3}$$

with $\phi = k_c a_L$. One can prove that $I_{m-n} = I^*_{n-m}$. If two laser drives with frequencies ω_0 and ω_1 are used to illuminate atoms trapped in a tilted system, and $\delta = m - n$, the full Hamiltonian describing the motion and internal dynamics of the atoms is given by

$$\begin{aligned} \hat{H}_{\rm lab}/\hbar &= \left(\frac{\Omega^c}{2} e^{-\mathbf{i}\omega_0 t} \sum_{l\delta} I_\delta e^{\mathbf{i}l\phi} \hat{c}^{\dagger}_{le} \hat{c}_{l+\delta g} + \text{h.c.} \right) \\ &+ \left(\frac{\Omega^s}{2} e^{-\mathbf{i}\omega_1 t} \sum_{l\delta} I_\delta e^{\mathbf{i}l\phi} \hat{c}^{\dagger}_{le} \hat{c}_{l+\delta g} + \text{h.c.} \right) \\ &- J \sum_{l\alpha} \hat{c}^{\dagger}_{l+1\alpha} c_{l\alpha} + \omega_a \sum_{l} \hat{c}^{\dagger}_{le} \hat{c}_{le} + \Delta \sum_{l\alpha} l \hat{c}^{\dagger}_{l\alpha} \hat{c}_{l\alpha}, \end{aligned} \tag{A4}$$

where $\hbar\Delta = M_a g_{\rm acc} a_L$ is the the potential energy difference between atoms at adjacent lattice sites. Rewritting the

Hamiltonian in terms of Wannier-Stark (WS) states, that diagonalize the motional degrees of freedom:

$$\hat{H}/\hbar = -J\sum_{l\alpha}\hat{c}^{\dagger}_{l+1\alpha}\hat{c}_{l\alpha} + \Delta\sum_{l\alpha} l\hat{c}^{\dagger}_{l\alpha}\hat{c}_{l\alpha} + \text{h.c.},$$

with $\hat{c}_{l\alpha} = \sum_m \mathcal{J}_{l-m}(2J/\Delta)\hat{\tilde{c}}_{m\alpha}$, we have [63]

$$\sum_l e^{\mathbf{i}l\phi}\hat{c}^{\dagger}_{le}\hat{c}_{l+\delta g} = \sum_{lk} e^{\mathbf{i}l\phi}\, e^{-\mathbf{i}(\delta-k)(\pi+\phi)/2}\mathcal{J}_{\delta-k}(\tilde{J})\hat{\tilde{c}}^{\dagger}_{le}\hat{\tilde{c}}_{l+kg}, \tag{A5}$$

where $\tilde{J} = 4J\,|\sin(\phi/2)|\,/\Delta$. As a result, $\hat{H}_{\text{lab}}/\hbar$ becomes

$$\begin{aligned}
&\hat{H}_{\text{lab}}/\hbar \\
&= \frac{\Omega^c}{2}\, e^{-\mathbf{i}\omega_0 t}\sum_{lk\delta} I_\delta\, e^{\mathbf{i}l\phi}\, e^{-\mathbf{i}(\delta-k)(\pi+\phi)/2}\mathcal{J}_{\delta-k}(\tilde{J})\hat{\tilde{c}}^{\dagger}_{le}\hat{\tilde{c}}_{l+kg} + \text{h.c.} \\
&\quad + \frac{\Omega^s}{2}\, e^{-\mathbf{i}\omega_1 t}\sum_{lk\delta} I_\delta\, e^{\mathbf{i}l\phi}\, e^{-\mathbf{i}(\delta-k)(\pi+\phi)/2}\mathcal{J}_{\delta-k}(\tilde{J})\hat{\tilde{c}}^{\dagger}_{le}\hat{\tilde{c}}_{l+kg} \\
&\quad + \text{h.c.} + \omega_a\sum_l \hat{\tilde{c}}^{\dagger}_{le}\hat{\tilde{c}}_{le} + \Delta\sum_{l\alpha} l\hat{\tilde{c}}^{\dagger}_{l\alpha}\hat{\tilde{c}}_{l\alpha}.
\end{aligned} \tag{A6}$$

Assuming that the lattice is deep enough that the Wannier states are mostly localized at a single lattice site, and that the carrier and sideband Rabi frequencies are weak and thus cannot drive undesirable transitions, we can set $\delta = 0$ and $k = 0$, and ignore other terms (see Appendix B when the $k = 0$ approximation is not assumed). In this case we obtain

$$\begin{aligned}
&\hat{H}_{\text{lab}}/\hbar \\
&\simeq \frac{\Omega^c I_0}{2} e^{-\mathbf{i}\omega_0 t}\sum_l \Big(e^{\mathbf{i}l\phi}\mathcal{J}_0(\tilde{J})\hat{\tilde{c}}^{\dagger}_{le}\hat{\tilde{c}}_{lg} \\
&\qquad + e^{\mathbf{i}l\phi}e^{\mathbf{i}(\pi+\phi)/2}\mathcal{J}_{-1}(\tilde{J})\hat{\tilde{c}}^{\dagger}_{le}\hat{\tilde{c}}_{l+1g}\Big) \\
&\quad + \frac{\Omega^s I_0}{2} e^{-\mathbf{i}\omega_1 t}\sum_l \Big(e^{\mathbf{i}l\phi}\mathcal{J}_0(\tilde{J})\hat{\tilde{c}}^{\dagger}_{le}\hat{\tilde{c}}_{lg} \\
&\qquad + e^{\mathbf{i}l\phi}e^{\mathbf{i}(\pi+\phi)/2}\mathcal{J}_{-1}(\tilde{J})\hat{\tilde{c}}^{\dagger}_{le}\hat{\tilde{c}}_{l+1g}\Big) \\
&\quad + \omega_a\sum_l \hat{\tilde{c}}^{\dagger}_{le}\hat{\tilde{c}}_{le} + \Delta\sum_{l\alpha} l\hat{\tilde{c}}^{\dagger}_{l\alpha}\hat{\tilde{c}}_{l\alpha}.
\end{aligned} \tag{A7}$$

APPENDIX B: AC STARK SHIFT IN WANNIER-STARK OLCS

The full Hamiltonian in the lab frame, when driving one of the sideband transitions, reads

$$\begin{aligned}
\hat{H}^s_{\text{lab}}/\hbar = \frac{\Omega^s I_0}{2} e^{-\mathbf{i}\omega_1 t}\sum_l \Big(&\mathcal{J}_0(\tilde{J})\hat{\tilde{c}}^{\dagger}_{le}\hat{\tilde{c}}_{lg} \\
&+ e^{\mathbf{i}(\pi+\phi)/2}\mathcal{J}_{-1}(\tilde{J})\hat{\tilde{c}}^{\dagger}_{le}\hat{\tilde{c}}_{l+1g}\Big) + \text{h.c.}
\end{aligned} \tag{B1}$$

Go to the rotating frame as mentioned in the main text, namely,

$$\hat{\tilde{c}}^{\dagger}_{le} \to e^{\mathbf{i}t[(\omega_0-\omega_1)l+\omega_0]}\hat{\tilde{c}}^{\dagger}_{le},\ \hat{\tilde{c}}^{\dagger}_{lg} \to e^{\mathbf{i}t(\omega_0-\omega_1)l}\hat{\tilde{c}}^{\dagger}_{lg}, \tag{B2}$$

when $\omega_0 - \omega_1 = \Delta$, we get

$$\begin{aligned}
\hat{H}^s_{\text{RF}}/\hbar = \frac{\Omega^s I_0}{2}\sum_l \Big(&e^{\mathbf{i}\Delta t}\mathcal{J}_0(\tilde{J})\hat{\tilde{c}}^{\dagger}_{le}\hat{\tilde{c}}_{lg} \\
&+ e^{\mathbf{i}\pi/2}\mathcal{J}_{-1}(\tilde{J})\hat{\tilde{c}}^{\dagger}_{le}\hat{\tilde{c}}_{l+1g}\Big) + \text{h.c.}
\end{aligned} \tag{B3}$$

Then we go to the rotating-gauge frame where all the couplings are real:

$$\begin{aligned}
&\hat{H}^s_{\text{RGF}}/\hbar \\
&= \frac{\Omega^s I_0}{2}\sum_l \Big(e^{\mathbf{i}\Delta t}\mathcal{J}_0(\tilde{J})\hat{a}^{\dagger}_{le}\hat{a}_{lg} + \mathcal{J}_{-1}(\tilde{J})\hat{a}^{\dagger}_{le}\hat{a}_{l+1g}\Big) + \text{h.c.} \\
&\simeq \frac{\Omega^s I_0\mathcal{J}_{-1}(\tilde{J})}{2}\sum_l \Big(\hat{a}^{\dagger}_{le}\hat{a}_{l+1g} + \text{h.c.}\Big) \\
&\quad - \frac{\left(\Omega^s I_0\mathcal{J}_0(\tilde{J})\right)^2}{4\Delta}\sum_l \Big(\hat{a}^{\dagger}_{lg}\hat{a}_{lg} - \hat{a}^{\dagger}_{le}\hat{a}_{le}\Big).
\end{aligned} \tag{B4}$$

The last line of the above equation accounts for the ac Stark shift. Similarly, we can repeat the above analysis for the carrier drive and obtain

$$\begin{aligned}
&\hat{H}^c_{\text{SSH}}/\hbar \\
&= \frac{\Omega^c I_0}{2}\sum_l \Big(\mathcal{J}_0(\tilde{J})\hat{a}^{\dagger}_{le}\hat{a}_{lg} + e^{-\mathbf{i}\Delta t}\mathcal{J}_{-1}(\tilde{J})\hat{a}^{\dagger}_{le}\hat{a}_{l+1g}\Big) + \text{h.c.} \\
&\simeq \frac{\Omega^c I_0\mathcal{J}_0(\tilde{J})}{2}\sum_l \Big(\hat{a}^{\dagger}_{le}\hat{a}_{lg} + \text{h.c.}\Big) \\
&\quad - \frac{\left(\Omega^c I_0\mathcal{J}_{-1}(\tilde{J})\right)^2}{4\Delta}\sum_l \Big(\hat{a}^{\dagger}_{le}\hat{a}_{le} - \hat{a}^{\dagger}_{lg}\hat{a}_{lg}\Big),
\end{aligned} \tag{B5}$$

In the the main text, we consider a shallow lattice with lattice depth $5E_r$, which gives us $J_0(\tilde{J})/J_1(\tilde{J}) \simeq 1.73$.

The above equations show that the ac Stark shift effectively adds to the system a detuning. When the laser interrogation time is relatively short, we can ignore the AC Stark shift terms if

$$\frac{\Omega^s I_0\mathcal{J}_{-1}(\tilde{J})}{2} \ll \frac{\left(\Omega^s I_0\mathcal{J}_0(\tilde{J})\right)^2}{4\Delta}$$

and

$$\frac{\Omega^c I_0\mathcal{J}_0(\tilde{J})}{2} \ll \frac{\left(\Omega^c I_0\mathcal{J}_{-1}(\tilde{J})\right)^2}{4\Delta},$$

or if $\Omega^c, \Omega^s \ll \Delta$. However, when the laser interrogation time is long, the ac Stark shift, especially the one related to the sideband drive, cannot be ignored.

APPENDIX C: ANALYTICAL DERIVATION OF $X(T)/a_L$ IN THE SSH MODEL

The SSH model in the quasimomentum space reads

$$\hat{H}_{\rm SSH}/\hbar = \sum_k \left(\frac{\Omega_A}{2} \hat{a}^\dagger_{ke} \hat{a}_{kg} + \frac{\Omega_B}{2} e^{-\mathbf{i}ka_L} \hat{a}^\dagger_{ke} \hat{a}_{kg} + \text{h.c.} \right), \tag{C1}$$

with eigenenergies

$$E_k^\pm = \pm E_k = \pm \frac{1}{2} \sqrt{\Omega_A^2 + \Omega_B^2 + 2\Omega_A \Omega_B \cos ka_L}$$

and eigenvectors

$$|k, \pm\rangle = \frac{1}{\sqrt{2}} \left(\pm e^{-\mathbf{i}\phi_k} \hat{a}^\dagger_{ke} + \hat{a}^\dagger_{kg} \right) |0\rangle , \tag{C2}$$

where

$$\tan \phi_k = \frac{\Omega_B \sin ka_L}{\Omega_A + \Omega_B \cos ka_L}.$$

The operator $\hat{I}_y$ and the initial state in k space are

$$\hat{I}_y = -\mathbf{i} \sum_k e^{-\mathbf{i}ka_L} \hat{a}^\dagger_{ke} \hat{a}_{kg} + \text{h.c.} \tag{C3}$$

and

$$\begin{aligned} |\psi_0\rangle = \hat{a}^\dagger_{0g} |0\rangle &= \frac{1}{\sqrt{L}} \sum_k \hat{a}^\dagger_{kg} |0\rangle \\ &= \frac{1}{\sqrt{2L}} \sum_k \left(|k, +\rangle - |k, -\rangle \right). \end{aligned} \tag{C4}$$

We thus obtain

$$\begin{aligned} I_y(t) &= -\mathbf{i} \langle 0 | \hat{a}_{kg} e^{\mathbf{i}\hat{H}t} \sum_p e^{-\mathbf{i}pa_L} \hat{a}^\dagger_{pe} \hat{a}_{pg} e^{-\mathbf{i}\hat{H}t} \hat{a}^\dagger_{kg} | 0 \rangle + \text{c.c.} \\ &= \frac{1}{2L} \sum_k \left(\frac{\Omega_A \cos ka_L + \Omega_B}{E_k^2} \right) \sin(2E_k t). \end{aligned} \tag{C5}$$

Thus

$$\begin{aligned} \frac{X(T)}{\Omega_B a_L} &= \int_0^T dt\, I_y(t) \\ &= \frac{1}{2L} \sum_k \left(\frac{\Omega_A \cos ka_L + \Omega_B}{E_k^2} \right) [1 - \cos(2E_k T)] \end{aligned} \tag{C6}$$

$$\xrightarrow{L\to\infty} \frac{a_L}{8\pi} \int_{-\pi}^{\pi} dk \left(\frac{\Omega_A \cos ka_L + \Omega_B}{E_k^2} \right) \times [1 - \cos(2E_k T)]. \tag{C7}$$

We identify the Berry phase from the above equation:

$$\mathcal{A}(k) \equiv -\frac{1}{2} \frac{d\phi_k}{dk} = -\frac{1}{2} \frac{a_L \Omega_B (\Omega_A \cos ka_L + \Omega_B)}{4E_k^2}, \tag{C8}$$

and recall the relation between Berry phase and the winding number, $\mathcal{W}$:

$$\mathcal{W} = -\frac{1}{\pi} \int_{BZ} \mathcal{A}(k)\, dk. \tag{C9}$$

Thus the winding number relates to $x(T)$ via

$$\frac{X(T)}{a_L} = \frac{\mathcal{W}_{\rm SSH}}{2} - \frac{1}{2} \int_{BZ} \frac{dk}{2\pi} \frac{d\phi_k}{dk} \cos(2E_k T). \tag{C10}$$

APPENDIX D: I_x IN THE PRESENCE OF SMALL δ, δ_t

We can use linear response theory and perturbation theory to understand the effect of nonzero but small detunnigs, δ and δ_t. Using $\hat{O} = \hat{O}_0 + \Delta\hat{O}$, where $\hat{O}_0$ is the unperturbed operator, and

$$\Delta\hat{O} \simeq \mathbf{i} \int_0^t ds \left[\Delta\hat{H}(s), \hat{O}(t) \right], \tag{D1}$$

where both $\Delta\hat{H}(s)$ and $\hat{O}(t)$ are in the Heisenberg picture of $H_{\rm SSH}$. We thus obtain for the case when the unperturbed Hamiltonian is the SSH model:

$$\Delta\hat{I}_x(t) = \mathbf{i} \int_0^t ds \left[\hat{U}^\dagger(s) \Delta\hat{U}(s), \hat{I}_x(t) \right], \tag{D2}$$

where $\hat{U}(s) = e^{-\mathbf{i}\hat{H}_{\rm SSH} s}$. When $\Delta\hat{H} = -\delta \sum_l \hat{S}_{lz}$,

$$\begin{aligned} \Delta\hat{I}_x(t) &= -\mathbf{i}\delta \int_0^t ds \left[\hat{U}^\dagger(s) \hat{\sum_l} \hat{S}_{lz} \hat{U}(s), \hat{U}^\dagger(t) \hat{I}_x \hat{U}^\dagger(t) \right] \\ &= \frac{\delta}{2L} \sum_k \frac{\cos(2E_k t) - 1}{2E_k} \left[e^{\mathbf{i}(-ka_L + \phi_k)} + \text{c.c.} \right] 2S_{kz}. \end{aligned} \tag{D3}$$

One can evaluate $\Delta I_x(t)$ with initial condition $|0\rangle = |0, g\rangle$, and obtain $I_x(t) \simeq \delta \mathcal{W}_{\rm SSH}/\Omega_B$. Similarly, when $\Delta\hat{H} = \delta_t \sum_{l,\alpha=e/g} l\hat{n}_{l\alpha}$, we also have $I_x(t) \propto \delta_t$. In this case,

$$\begin{aligned} &\int_0^t ds \left[\hat{U}^\dagger(s) \sum_{l,\alpha=e/g} l\hat{n}_{l\alpha} \hat{U}(s), \hat{U}^\dagger(t) \hat{I}_x \hat{U}^\dagger(t) \right] \\ &\quad \equiv S(\Omega_A, \Omega_B, t) \equiv \tilde{S}(\Omega_A, \Omega_B) + \text{osc. term}, \end{aligned} \tag{D4}$$

where $S(\Omega_A, \Omega_B, t), \tilde{S}(\Omega_A, \Omega_B) \neq 0$ but does not have a direct relation with $\mathcal{W}_{\rm SSH}$. We plot the numerically evaluated result for $S(\Omega_A, \Omega_B, t)$ in Fig. 8.

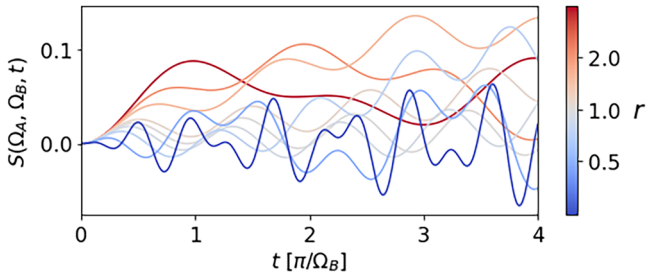

FIG. 8. Numerical results for $S(\Omega_A, \Omega_B, t)$. Here we fix $\Omega_B/(2\pi) = 10\,\mathrm{Hz}$ and vary r values.

APPENDIX E: ALTERNATIVE PROTOCOL FOR THE SSH CLOCK SPECTROSCOPY

We show in Fig. 9 an alternative protocol for the SSH clock spectroscopy. In this protocol, we first adiabatically prepare an initial condition $(|0,g\rangle + |-1,e\rangle)/\sqrt{2}$, then turn on the RM dynamics for time $t_B = \pi/\Omega_B$, followed by measuring $-S_z$. In fact, with this protocol, we can analytically obtain $S_z(t) = -I_x(t)$, where I_x is precisely given by the results in Appendix D.

We would like to note that, a combination of adiabatic state preparation, the initial state, and S_z measurement at the end of the protocol could in principle reduce the statistical noise caused by experimental imperfections.

APPENDIX F: TOPOLOGICAL PHASE TRANSITION IN FINITE-SIZE CHAINS

In this section, we briefly study the finite-size effects on the topological phase transition. As discussed in the main text and prior appendices, the sideband coherence of

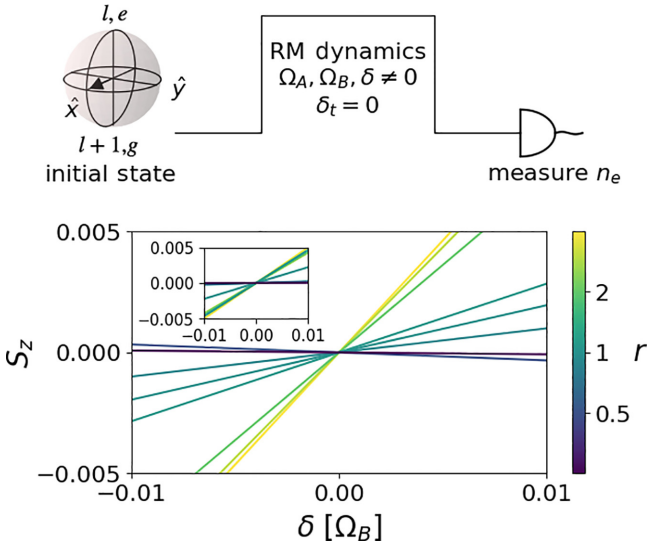

FIG. 9. Alternative SSH clock spectroscopy. Upper panel: the protocol. Lower panel: numerical simulation.

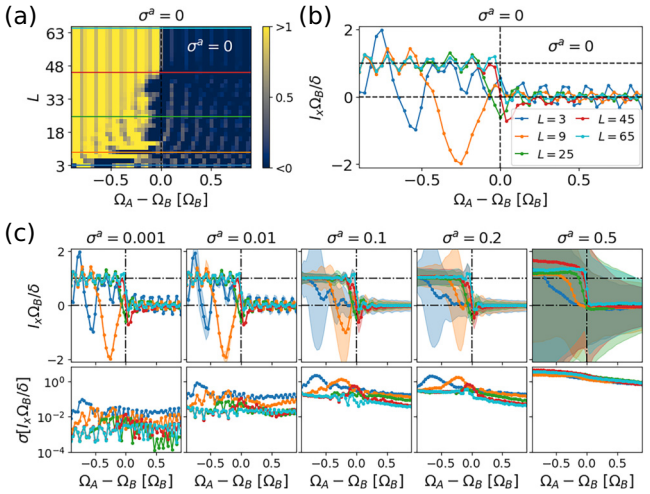

FIG. 10. Topological phase transition, as indicated by $I_x\Omega_B/\delta$, in a finite chain with length L. We vary Ω_A values, fix $t\Omega_B = 15\pi$, $\Omega_B/(2\pi) = 10\,\mathrm{Hz}$, and $\delta = 0.01\Omega_B$. (a),(b) Noise-free results of $I_x\Omega_B/\delta$ with different $\Omega_A - \Omega_B$ and L values. (a) $I_x\Omega_B/\delta$ vs L and $\Omega_A - \Omega_B$. (b) Several cross sections of panel (a), as indicated by colors. (c) $I_x\Omega_B/\delta$ in the presence of shot-to-shot amplitude noise of $\Omega_{A/B}$ with standard deviation $\sigma_a\Omega_{A/B}$, where $\sigma_a = 0.001, 0.01, 0.1, 0.2$, and 0.5. Upper panels: same as (b), but over 500 realizations of noise, with solid curves showing the average value while shaded areas indicate the standard deviation. Lower panels: values of the standard deviation of the upper panels for better visualization.

a RM chain relates to the winding number of its underlying SSH model via $I_x\Omega_B/\delta = \mathcal{W}_{\mathrm{SSH}}$. This conclusion, however, assumes an infinite SSH (RM) chain with periodic boundary condition. Here we discuss the breakdown of this assumption when in reality we have the open boundary condition and finite-size chains. We also discuss how $I_x\Omega_B/\delta = \mathcal{W}_{\mathrm{SSH}}$ behaves with and without shot-to-shot uncertainty of Ω_A, Ω_B, via numerical calculations of $I_x(t)$ at $t\Omega_B = 15\pi$, with fixed Ω_B and $\delta = 0.01\Omega_B$ values.

We show in Figs. 10(a) and 10(b) how $I_x\Omega_B/\delta$ varies for different total number of lattice sites L, with initial state being a single atom at g internal state at the center site of the chain. When L is small, the range of $|\Omega_A - \Omega_B|$ values, within which $I_x\Omega_B/\delta$ changes from 1 to 0, is very large. As L increases, this range reduces. In our simulation, we observe that for $L > 45$, the transition of $I_x\Omega_B/\delta$ becomes very sharp. The energy spectrum of the underlying SSH model is always gapped when $\Omega_A < \Omega_B$ and when $\Omega_A > \Omega_B$. The energy gap only closes when $\Omega_A = \Omega_B$ as $L \to \infty$. The distinct behavior of $I_x\Omega_B/\delta$ in the regimes $\Omega_A < \Omega_B$ and $\Omega_A > \Omega_B$ is not a consequence of the gap but instead a result of a topological phase transition: such transition happens only in the presence of gap closing (when $L \to \infty$), and the symmetry of the system remains unchanged before and after the phase transition.

In the presence of shot-to-shot amplitude variations of the Rabi frequency. $I_x\Omega_B/\delta$ behaves qualitatively similar to the noise-free case Fig. 10(b), but as shown in Fig. 10(c), the standard deviation in $\sigma[I_x\Omega_B/\delta]$ increases as indicated by the shaded areas in the upper panels and their corresponding lower panels. While $\sigma[I_x\Omega_B/\delta]$ increases with increasing noise variance σ_a, as expected, its fluctuation reduces as L increases. Such behavior persists until σ_a is as large as 0.5, when the noise is so large that it breaks such protection.

In summary, we have shown in this Appendix that, (1) as L increases, the window of $|\Omega_A - \Omega_B|$ values within which $I_x\Omega_B/\delta$ changes between 0 and 1 reduces, i.e., as L increases, the topological phase transition becomes sharper; (2) at a fixed time, as L becomes large enough (in the case here, $L > 45$), a topological phase transition can be observed and when deep in the topological phase, $I_x\Omega_B/\delta$ is less impacted by small uncertainties of Ω_A, Ω_B, until such uncertainties become too large to be considered as a perturbation.

APPENDIX G: FULL SENSITIVITY COMPARISON BETWEEN TWO CLOCK SPECTROSCOPY PROTOCOLS

In this section, we compare the sensitivity of our SSH spectroscopy protocol to that of the Rabi spectroscopy protocol. Since the laser interrogation of our protocol is 5 times that of the Rabi protocol, we need to compare one measurement in our protocol to five measurements of the Rabi protocol.

In the presence of N noninteracting atoms and a global noise with standard deviation σ, the sensitivity of measuring an observable $O = \sum_i O_i$ where O_i is a single particle observable, for m times, is given by

$$\Delta^2\delta_1 = \frac{mN/4 + m\gamma_1^2\sigma^2N^2}{m^2(dO/d\delta)^2} = \frac{1}{4mN\alpha_1^2} + \frac{\gamma_1^2\sigma^2}{m\alpha_1^2}, \quad \text{(G1)}$$

where $dO/d\delta = N\alpha_1$, and γ_1 is how O varies in the presence of noise with standard deviation σ, or $\partial O/\partial\Omega$ in our case.

When $m = 1$, the above expression becomes

$$\Delta^2\delta_2 = \frac{N/4 + \gamma_2^2\sigma^2N^2}{(dO'/d\delta)^2} = \frac{1}{4N\alpha_2^2} + \frac{\gamma_2^2\sigma^2}{\alpha_2^2}, \quad \text{(G2)}$$

where $dO'/d\delta = N\alpha_2$. For Protocol 2 to have better sensitivity than Protocol 1 when $\Delta^2\delta_1 > \Delta^2\delta_2$, we need

$$\left[\left(\frac{\gamma_1}{\gamma_2}\right)^2\frac{\beta^2}{m} - 1\right]N > \frac{1}{4\sigma^2\gamma_2^2}\left(1 - \frac{\beta^2}{m}\right), \quad \text{(G3)}$$

where $\beta = \alpha_2/\alpha_1$. When we have two protocols with comparable signal and when $\gamma_1 \gg \gamma_2$, the above equation becomes

$$N > \frac{m - \beta^2}{4\sigma^2(\gamma_1^2\beta^2 - m\gamma_2^2)}. \quad \text{(G4)}$$

When Protocol 1 is the Rabi spectroscopy and Protocol 2 is the SSH spectroscopy, we have $\sigma = 0.001$, $\beta \simeq 0.6$, $m = 5$, $\gamma_2^2 \simeq 0.00027$, $\gamma_1^2 \simeq 0.035$, resulting in $N > 10^8$ atoms. Namely, in the presence of over 10^8 atoms, the SSH protocol has better sensitivity.

We would like to additionally comment that, if both protocols have the same $dO/d\delta$, i.e., $\beta = 1$, while all other quantities remain unchanged, we have $N > 3 \times 10^7$. If $m = 1$, while all other quantities remain unchanged, we have $N > 1.5 \times 10^7$.

[1] T. L. Nicholson, S. L. Campbell, R. B. Hutson, G. E. Marti, B. J. Bloom, R. L. McNally, W. Zhang, M. D. Barrett, M. S. Safronova, G. F. Strouse, W. L. Tew, and J. Ye, Systematic evaluation of an atomic clock at 2×10^{-18} total uncertainty, Nat. Commun. **6**, 6896 (2015).

[2] Andrew D. Ludlow, Martin M. Boyd, Jun Ye, E. Peik, and P. O. Schmidt, Optical atomic clocks, Rev. Mod. Phys. **87**, 637 (2015).

[3] S. L. Campbell, R. B. Hutson, G. E. Marti, A. Goban, N. Darkwah Oppong, R. L. McNally, L. Sonderhouse, J. M. Robinson, W. Zhang, B. J. Bloom, and J. Ye, A Fermi-degenerate three-dimensional optical lattice clock, Science **358**, 90 (2017).

[4] W. F. McGrew, X. Zhang, R. J. Fasano, S. A. Schäffer, K. Beloy, D. Nicolodi, R. C. Brown, N. Hinkley, G. Milani, M. Schioppo, T. H. Yoon, and A. D. Ludlow, Atomic clock performance enabling geodesy below the centimetre level, Nature **564**, 87 (2018).

[5] E. Oelker, R. B. Hutson, C. J. Kennedy, L. Sonderhouse, T. Bothwell, A. Goban, D. Kedar, C. Sanner, J. M. Robinson, G. E. Marti, D. G. Matei, T. Legero, M. Giunta, R. Holzwarth, F. Riehle, U. Sterr, and J. Ye, Demonstration of 4.8×10^{-17} stability at 1 s for two independent optical clocks, Nat. Photonics **13**, 714 (2019).

[6] Tobias Bothwell, Colin J. Kennedy, Alexander Aeppli, Dhruv Kedar, John M. Robinson, Eric Oelker, Alexander Staron, and Jun Ye, Resolving the gravitational redshift across a millimetre-scale atomic sample, Nature **602**, 420 (2022).

[7] Xin Zheng, Jonathan Dolde, Varun Lochab, Brett N. Merriman, Haoran Li, and Shimon Kolkowitz, Differential clock comparisons with a multiplexed optical lattice clock, Nature **602**, 425 (2022).

[8] Alexander Aeppli, Anjun Chu, Tobias Bothwell, Colin J. Kennedy, Dhruv Kedar, Peiru He, Ana Maria Rey, and Jun Ye, Hamiltonian engineering of spin-orbit–coupled fermions in a Wannier-Stark optical lattice clock, Sci. Adv. **8**, eadc9242 (2022).

[9] Kyle Beloy *et al.*, Frequency ratio measurements at 18-digit accuracy using an optical clock network, Nature **591**, 564 (2021).

[10] Alexander Aeppli, Kyungtae Kim, William Warfield, Marianna S. Safronova, and Jun Ye, Clock with 8×10^{-19} systematic uncertainty, Phys. Rev. Lett. **133**, 023401 (2024).

[11] N. R. Cooper, J. Dalibard, and I. B. Spielman, Topological bands for ultracold atoms, Rev. Mod. Phys. **91**, 015005 (2019).

[12] Roberta Citro and Monika Aidelsburger, Thouless pumping and topology, Nat. Rev. Phys. **5**, 87 (2023).

[13] W. P. Su, J. R. Schrieffer, and A. J. Heeger, Solitons in polyacetylene, Phys. Rev. Lett. **42**, 1698 (1979).

[14] W. P. Su, J. R. Schrieffer, and A. J. Heeger, Soliton excitations in polyacetylene, Phys. Rev. B **22**, 2099 (1980).

[15] M. J. Rice and E. J. Mele, Elementary excitations of a linearly conjugated diatomic polymer, Phys. Rev. Lett. **49**, 1455 (1982).

[16] Marcos Atala, Monika Aidelsburger, Julio T. Barreiro, Dmitry Abanin, Takuya Kitagawa, Eugene Demler, and Immanuel Bloch, Direct measurement of the Zak phase in topological Bloch bands, Nat. Phys. **9**, 795 (2013).

[17] M. Lohse, C. Schweizer, O. Zilberberg, M. Aidelsburger, and I. Bloch, A Thouless quantum pump with ultracold bosonic atoms in an optical superlattice, Nat. Phys. **12**, 350 (2016).

[18] Shuta Nakajima, Takafumi Tomita, Shintaro Taie, Tomohiro Ichinose, Hideki Ozawa, Lei Wang, Matthias Troyer, and Yoshiro Takahashi, Topological Thouless pumping of ultracold fermions, Nat. Phys. **12**, 296 (2016).

[19] Anne-Sophie Walter, Zijie Zhu, Marius Gächter, Joaquín Minguzzi, Stephan Roschinski, Kilian Sandholzer, Konrad Viebahn, and Tilman Esslinger, Quantization and its breakdown in a Hubbard–Thouless pump, Nat. Phys. **19**, 1471 (2023).

[20] Eric J. Meier, Fangzhao Alex An, and Bryce Gadway, Observation of the topological soliton state in the Su-Schrieffer-Heeger model, Nat. Commun. **7**, 13986 (2016).

[21] Eric J. Meier, Fangzhao Alex An, Alexandre Dauphin, Maria Maffei, Pietro Massignan, Taylor L. Hughes, and Bryce Gadway, Observation of the topological Anderson insulator in disordered atomic wires, Science **362**, 929 (2018).

[22] Tao Yuan, Chao Zeng, Yi-Yi Mao, Fei-Fei Wu, Yan-Jun Xie, Wen-Zhuo Zhang, Han-Ning Dai, Yu-Ao Chen, and Jian-Wei Pan, Realizing robust edge-to-edge transport of atomic momentum states in a dynamically modulated synthetic lattice, Phys. Rev. Res. **5**, L032005 (2023).

[23] Sylvain de Léséleuc, Vincent Lienhard, Pascal Scholl, Daniel Barredo, Sebastian Weber, Nicolai Lang, Hans Peter Büchler, Thierry Lahaye, and Antoine Browaeys, Observation of a symmetry-protected topological phase of interacting bosons with Rydberg atoms, Science **365**, 775 (2019).

[24] S. K. Kanungo, J. D. Whalen, Y. Lu, M. Yuan, S. Dasgupta, F. B. Dunning, K. R. A. Hazzard, and T. C. Killian, Realizing topological edge states with Rydberg-atom synthetic dimensions, Nat. Commun. **13**, 972 (2022).

[25] Martin Leder, Christopher Grossert, Lukas Sitta, Maximilian Genske, Achim Rosch, and Martin Weitz, Real-space imaging of a topologically protected edge state with ultracold atoms in an amplitude-chirped optical lattice, Nat. Commun. **7**, 13112 (2016).

[26] Or Katz, Lei Feng, Diego Porras, and Christopher Monroe, Observing topological insulator phases with a programmable quantum simulator, ArXiv:2401.10362 [quant-ph].

[27] Dizhou Xie, Wei Gou, Teng Xiao, Bryce Gadway, and Bo Yan, Topological characterizations of an extended Su-Schrieffer-Heeger model, npj Quantum Inf. **5**, 55 (2019).

[28] H.-I Lu, M. Schemmer, L. M. Aycock, D. Genkina, S. Sugawa, and I. B. Spielman, Geometrical pumping with a Bose-Einstein condensate, Phys. Rev. Lett. **116**, 200402 (2016).

[29] J. Zak, Berry's phase for energy bands in solids, Phys. Rev. Lett. **62**, 2747 (1989).

[30] S. Kolkowitz, S. L. Bromley, T. Bothwell, M. L. Wall, G. E. Marti, A. P. Koller, X. Zhang, A. M. Rey, and J. Ye, Spin–orbit-coupled fermions in an optical lattice clock, Nature **542**, 66 (2017).

[31] Cristian D. Panda, Matthew J. Tao, Miguel Ceja, Justin Khoury, Guglielmo M. Tino, and Holger Müller, Measuring gravitational attraction with a lattice atom interferometer, Nature **631**, 515 (2024).

[32] B. Pelle, A. Hilico, G. Tackmann, Q. Beaufils, and F. Pereira dos Santos, State-labeling Wannier-Stark atomic interferometers, Phys. Rev. A **87**, 023601 (2013).

[33] Anjun Chu, Peiru He, James K. Thompson, and Ana Maria Rey, Quantum enhanced cavity QED interferometer with partially delocalized atoms in lattices, Phys. Rev. Lett. **127**, 210401 (2021).

[34] Lingfeng Yan, Stefan Lannig, William R. Milner, Max N. Frankel, Ben Lewis, Dahyeon Lee, Kyungtae Kim, and Jun Ye, A high-power clock laser spectrally tailored for high-fidelity quantum state engineering, ArXiv:2501.09343 [physics.atom-ph].

[35] S. Blatt, J. W. Thomsen, G. K. Campbell, A. D. Ludlow, M. D. Swallows, M. J. Martin, M. M. Boyd, and J. Ye, Rabi spectroscopy and excitation inhomogeneity in a one-dimensional optical lattice clock, Phys. Rev. A **80**, 052703 (2009).

[36] Kyungtae Kim, Alexander Aeppli, Tobias Bothwell, and Jun Ye, Evaluation of lattice light shift at low 10^{-19} uncertainty for a shallow lattice sr optical clock, Phys. Rev. Lett. **130**, 113203 (2023).

[37] Pierre Lemonde and Peter Wolf, Optical lattice clock with atoms confined in a shallow trap, Phys. Rev. A **72**, 033409 (2005).

[38] Michael L. Wall, Andrew P. Koller, Shuming Li, Xibo Zhang, Nigel R. Cooper, Jun Ye, and Ana Maria Rey, Synthetic spin-orbit coupling in an optical lattice clock, Phys. Rev. Lett. **116**, 035301 (2016).

[39] L. F. Livi, G. Cappellini, M. Diem, L. Franchi, C. Clivati, M. Frittelli, F. Levi, D. Calonico, J. Catani, M. Inguscio, and L. Fallani, Synthetic dimensions and spin-orbit coupling with an optical clock transition, Phys. Rev. Lett. **117**, 220401 (2016).

[40] Shanchao Zhang and Gyu-Boong Jo, Recent advances in spin-orbit coupled quantum gases, J. Phys. Chem. Solids **128**, 75 (2019).

[41] Simon Wili, Tilman Esslinger, and Konrad Viebahn, An accordion superlattice for controlling atom separation in optical potentials, New J. Phys. **25**, 033037 (2023).
[42] D. J. Thouless, Quantization of particle transport, Phys. Rev. B **27**, 6083 (1983).
[43] Q. Niu and D. J. Thouless, Quantised adiabatic charge transport in the presence of substrate disorder and many-body interaction, J. Phys. A: Math. Gen. **17**, 2453 (1984).
[44] Di Xiao, Ming-Che Chang, and Qian Niu, Berry phase effects on electronic properties, Rev. Mod. Phys. **82**, 1959 (2010).
[45] R. Wang and Z. Song, Robustness of the pumping charge to dynamic disorder, Phys. Rev. B **100**, 184304 (2019).
[46] Alexander Impertro, Simon Karch, Julian F. Wienand, SeungJung Huh, Christian Schweizer, Immanuel Bloch, and Monika Aidelsburger, Local readout and control of current and kinetic energy operators in optical lattices, Phys. Rev. Lett. **133**, 063401 (2024).
[47] M. S. Rudner and L. S. Levitov, Topological transition in a non-Hermitian quantum walk, Phys. Rev. Lett. **102**, 065703 (2009).
[48] Filippo Cardano, Alessio D'Errico, Alexandre Dauphin, Maria Maffei, Bruno Piccirillo, Corrado de Lisio, Giulio de Filippis, Vittorio Cataudella, Enrico Santamato, Lorenzo Marrucci, Maciej Lewenstein, and Pietro Massignan, Detection of Zak phases and topological invariants in a chiral quantum walk of twisted photons, Nat. Commun. **8**, 15516 (2017).
[49] Maria Maffei, Alexandre Dauphin, Filippo Cardano, Maciej Lewenstein, and Pietro Massignan, Topological characterization of chiral models through their long time dynamics, New J. Phys. **20**, 013023 (2018).
[50] Bernd Lücke, Jan Peise, Giuseppe Vitagliano, Jan Arlt, Luis Santos, Géza Tóth, and Carsten Klempt, Detecting multiparticle entanglement of Dicke states, Phys. Rev. Lett. **112**, 155304 (2014).
[51] Lucas Gabardos, Bihui Zhu, Steven Lepoutre, Ana Maria Rey, Bruno Laburthe-Tolra, and Laurent Vernac, Relaxation of the collective magnetization of a dense 3D array of interacting dipolar S =3 atoms, Phys. Rev. Lett. **125**, 143401 (2020).
[52] Achim Peters, Keng Yeow Chung, and Steven Chu, Measurement of gravitational acceleration by dropping atoms, Nature **400**, 849 (1999).
[53] G. Rosi, F. Sorrentino, L. Cacciapuoti, M. Prevedelli, and G. M. Tino, Precision measurement of the Newtonian gravitational constant using cold atoms, Nature **510**, 518 (2014).
[54] P. Cladé, S. Guellati-Khélifa, C. Schwob, F. Nez, L. Julien, and F. Biraben, A promising method for the measurement of the local acceleration of gravity using Bloch oscillations of ultracold atoms in a vertical standing wave, Europhys. Lett. **71**, 730 (2005).
[55] Renée Charrière, Malo Cadoret, Nassim Zahzam, Yannick Bidel, and Alexandre Bresson, Local gravity measurement with the combination of atom interferometry and Bloch oscillations, Phys. Rev. A **85**, 013639 (2012).
[56] Xian Zhang, Ruben Pablo del Aguila, Tommaso Mazzoni, Nicola Poli, and Guglielmo M. Tino, Trapped-atom interferometer with ultracold Sr atoms, Phys. Rev. A **94**, 043608 (2016).
[57] Victoria Xu, Matt Jaffe, Cristian D. Panda, Sofus L. Kristensen, Logan W. Clark, and Holger Müller, Probing gravity by holding atoms for 20 seconds, Science **366**, 745 (2019).
[58] Cristian D. Panda, Matthew Tao, James Egelhoff, Miguel Ceja, Victoria Xu, and Holger Müller, Coherence limits in lattice atom interferometry at the one-minute scale, Nat. Phys. **20**, 1234 (2024).
[59] Holger Müller, Sheng-wey Chiow, Quan Long, Sven Herrmann, and Steven Chu, Atom interferometry with up to 24-photon-momentum-transfer beam splitters, Phys. Rev. Lett. **100**, 180405 (2008).
[60] Wenjie Liu, Yongguan Ke, and Chaohong Lee, Shortcuts to adiabatic Thouless pumping, ArXiv:2401.17081.
[61] Y.-T. Lin, D. M. Kennes, M. Pletyukhov, C. S. Weber, H. Schoeller, and V. Meden, Interacting Rice-Mele model: Bulk and boundaries, Phys. Rev. B **102**, 085122 (2020).
[62] Lintao Li, William Huie, Neville Chen, Brian DeMarco, and Jacob P. Covey, Active cancellation of servo-induced noise on stabilized lasers via feedforward, Phys. Rev. Appl. **18**, 064005 (2022).
[63] $\sum_k \mathcal{J}_{\nu+k}(u)\mathcal{J}_k(u)e^{\mathbf{i}k\alpha} = \mathcal{J}_\nu\left(2u\sin\left(\frac{\alpha}{2}\right)\right)e^{-\mathbf{i}\nu(\pi+\alpha)/2}$.